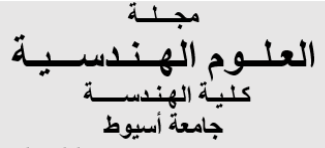


Journal of Engineering Sciences Faculty of Engineering Assiut University

JES





journal homepage: http://jesaun.journals.ekb.eg

Design and Implementation of A Radio Frequency Energy Harvesting (RF-EH) System in the WI-FI Band

Received 19 July 2025; Revised 16 September 2025; Accepted 17 September 2025

Ahmed Kabeel¹

Keywords

Radio Frequency Energy Harvesting (RF-EH), power divider, Microstrip Antenna Array, RF-to-DC Conversion Efficiency, Wi-Fi Band Energy

Abstract: The design and construction of radio frequency energy harvesting system (RF-EH) with of a 2.45 GHz specifically for Wi-Fi spectrum applications is presented in this paper. The proposed RF-EH system integrates three primary components: a circular-shaped microstrip antenna array, an equal-power combiner, and an FR-4 based RF-to-DC rectifier circuit. the antenna array was specifically built to improve signal reception, attained a measured gain of 15.8 dB, while the rectifier offered effective RF-to-DC conversion with a peak power conversion efficiency of 24.03% at an input power of 1.3 dBm. These elements work together to efficiently capture ambient Wi-Fi signals and make it evident that lowpower wireless sensor and Internet of Things devices can be powered by such systems. This energy harvesting system (RF-EH) has the potential to be a viable and useful alternative energy source for next-generation wireless communication applications because of its small size, reliance on the inexpensive FR-4 substrate, and smooth integration of antenna and rectifier design.

1. Introduction

The domain of Radio Frequency-Energy Harvesting (RF-EH) has gathered major consideration in this era of widespread wireless technology usage. Due to its significance in providing easy, cost-free energy for critical and hard-to-reach applications, it has become one of the most extensively studied topics globally, in general energy harvesting comprises capturing energy from numerous sources such as solar, light, thermal, wind, and kinetic energy, in the radio frequency (RF) spectrum, electromagnetic radiation can be converted into electrical energy, a process known as RF-EH [1].

Gadgets like sensors, wireless transmitters and receivers, plus a bunch of Internet of Things devices, totally depend on this tech [2]. The function of radio frequency energy harvesting (RF-EH) involves the conversion of RF signals into direct current electricity. This extracted energy can be stored for later utilization in storage solutions such as capacitors or batteries. Both smaller devices like wearables and medical implants as well as bigger systems like

¹Dept. of Electronics and Communication, Delta University for Science and Technolog, Egypt. ahmed.kabeel@deltauniv.edu.eg

those found in smart cities have benefited from the application of this technology. Receiving antennas, matching circuits, rectification circuits with low-pass filters, and energy storage mechanisms are the four basic parts of an RF-EH module [3] [4]. The ability of the harvester process to convert ambient radiofrequency energy into direct current power is what determines how efficient it is. When it comes to catching radio frequency signals from a particular frequency range and polarization, the antenna is essential. Radar imaging, medical imaging, cognitive radio systems, and high-data-rate personal area networks are just a few of the many uses for microstrip antennas [5]. Achieving high gain-bandwidth performance and compact size while maintaining cheap costs is the main problem in antenna design [6]. Numerous broadband antenna designs have been developed as a result of recent advances [7]. Rectifier circuits are necessary to transform intercepted radio frequencies into DC power that can be used. This section discusses the several rectifier topologies that are used in RF EH, including as voltage multiplier circuits, voltage doubler circuits, and rectifiers based on Schottky diodes. Performance of the entire system is directly impacted by the rectifier's efficiency. For RF-EH systems to operate dependably and to maximize the amount of energy captured, efficient power management is essential. Additionally, this section examines various power management tactics, including load management strategies, super capacitors, batteries, and maximum power point tracking (MPPT) algorithms. The antenna of an EH system is essential for absorbing ambient energy and should ideally have characteristics like small size, insensitivity to polarization, and a broad reception angle. Metamaterials have shown great promise as a replacement for traditional antennas recently, with the primary benefit being increased efficiency. Metamaterials are made up of arrays of tiny electrically resonant components that are usually arranged in two or three-dimensional structures like complementary split-ring resonators (CSRR) [8,9], and split-ring resonators (SRR) [10]. Metamaterials can absorb electromagnetic (EM) radiation at particular frequencies thanks to these resonant features. By adjusting the effective permittivity and permeability of the material to align with the input impedance of free space, you can significantly enhance absorption efficiency. This optimization not only improves performance but also maximizes the material's capabilities in practical applications. Embrace this approach for superior results. Though they are both built on the idea of perfect absorption, metamaterial absorbers and energy harvesters differ greatly from one another. The majority of the energy collected in absorption applications is dissipated inside the structure as ohmic or dielectric heat [11-14]. On the other hand, a network is utilized for EH purposes in order to collect the energy that is captured by several resonators and transfer it to a rectifier circuit [9, 10]. As a result, each unit cell in a metamaterial harvester design usually has one or more grounded resistors [15, 16]. Current metamaterial absorber designs disperse the absorbed energy into lumped resistors positioned in between the resonator's parts. Because these resistors are not grounded, it is difficult to integrate a power combining network [17–20]. In [8], the idea of employing metamaterial elements as energy gatherers for RF-EH was presented. It demonstrated how the terminals of metamaterial harvesters may capture and recycle electromagnetic power by means of

resistive loads. In addition, a number of metamaterial energy harvester types, including as wide-band [21,22], multi-polarization [23,24], polarization-insensitive, wide-incident angle [25,26], and multi-band designs [27–30], have been created to increase their applicability. The enhancement of electromagnetic (EM) energy harvesting performance is fundamentally linked to designs capable of capturing EM power regardless of the angle of incoming waves. Notably, multi-band designs are advantageous as they facilitate the collection of energy from a wider range of radiation sources. A critical factor to consider in metamaterialenabled energy harvesters is the efficiency of power conversion. To optimize this efficiency, a corporate feed network is employed to connect all components of the harvesting array to a unified load [31-36]. In the given context, four indistinguishable split-ring resonators (SRRs) were strategically situated within each segment of a triple-band meta surface resonator. These SRRs were integrated with resistive loads via quad harvesting ports, also known as vias. This configuration allows for an expansive reception angle, as evidenced by the research presented in reference [37,38]. Under normal conditions, the device exhibited energy harvesting efficiencies around 30% at a frequency of 1.75 GHz, 90% at 3.8 GHz, and 74% at 5.4 GHz. Nonetheless, in practical applications of harvesting systems, the combining network tends to experience reduced efficiency and increased complexity. This is mainly due to the distribution of power from each cell across multiple loads. In addition, a range of closed ring resonators in the shape of butterflies was used to create a metasurface for wide-ranging-angle, triple-band EM EH [39,40]. Harvesting efficiencies of 90%, 83%, and 81% were recorded at frequencies of 0.9 GHz, 2.6 GHz, and 5.7 GHz, respectively. Notably, the input impedances of the microwave power combining networks in these systems exhibit significant variation from the approximately 3 k Ω load resistance that is optimal for achieving such high efficiencies[41]. This discrepancy limits their applicability in practical energy harvesting scenarios. Recent developments in resonator design include the implementation of a ring resonator featuring dual resistive loads, as well as a symmetric electric-inductive capacitive (ELC) resonator that incorporates dual edge capacitances. These innovations contribute to the design of a dual-band metasurface resonator. [42,43]. to enhance harvesting efficiency, the metasurface underwent a process of pixilation, accompanied by the implementation of a binary optimization technique. There have been reports of 90% efficiency at 2.45 GHz and 6 GHz. It is important to keep in mind, nevertheless, that the majority of multi-band metamaterial harvesters have many harvesting ports (vias) for capturing electromagnetic energy and sending it to a load. This adds to the complexity, expense, and challenge of fabricating a corporate feed network. Figure 1 shows the design of an RF-EH system for little-power applications in this paper.

This planned EH system offers a reliable source of renewable electrical power for various applications. In this study, the antenna array is designed at 2.45 GHz using CST Microwave Studio software and implemented on an FR-4 substrate with $\varepsilon r = 4.3$ and h = 1.6 mm. Simulations showed that the planned circular antenna array organization exhibits great performance, delivering a gain of approximately 15.8 dBi, excessive efficiency, and the capability to gather RF power from all directions thanks to its omnidirectional radiation

pattern. An equal power combiner, an RF rectifier circuit, and a microstrip patch antenna array with a circular ground plane and rectangular patch antenna elements make up the system's three primary parts. The suggested antenna array runs at 2.45 GHz and is tailored for Wi-Fi applications. The simulated realized gain reaches 4.055 dBi at this frequency. Offering a wide bandwidth, an omnidirectional radiation pattern, and a respectable realized gain, the suggested array is a strong contender for EH. A circular sector equal power combiner operating at the same frequency of 2.45 GHz has been constructed to combine the RF energy from the antenna array. So as to guarantee impedance matching among the rectifier circuit and the power combiner, a matching circuit was also designed and built. The power combiner's captured RF energy is transformed into DC power by the rectifier circuit. With a load resistance of 200 Ω and a DC output voltage of 250 mV, the planned system's measured maximum RF-to-DC conversion efficiency is roughly 24.03%. The developed framework links to three goals of the United Nations Sustainable Development Goals (SDGs). First of all, it contributes to SDG 7: Ensure Access to Affordable, Reliable, Sustainable and Modern Energy for all by enabling the harvesting of renewable energy from ambient radio frequency sources. This kind of system also addresses SDG 9: Build Resilient Infrastructure, Promote Inclusive and Sustainable Industrialization and Foster Innovation as an innovative design of a reliable, self-sufficient wireless power transmission system, which has a potential benefit to society. Overall, the RF-EH system contributes to the advancement of clean forms of energy and of industries, responsible consumption and production patterns.

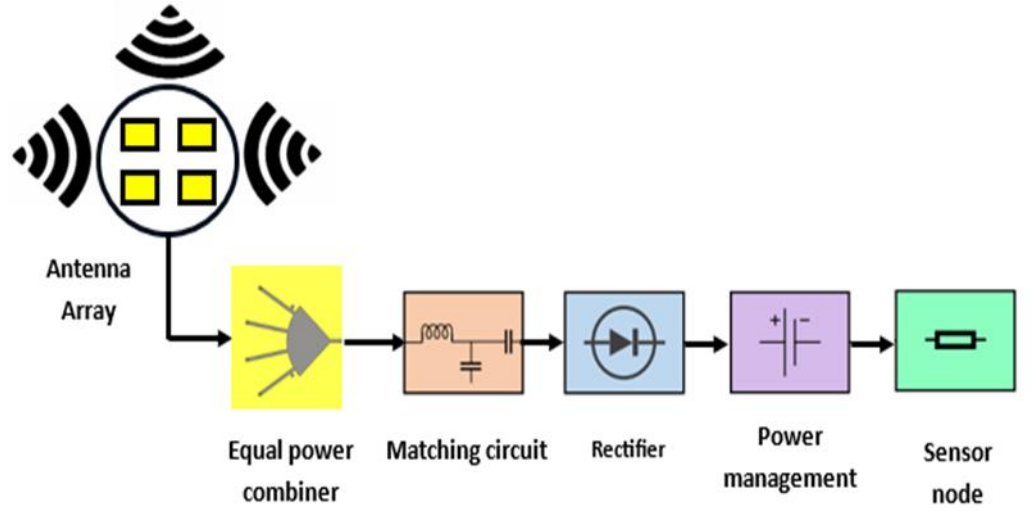


Figure 1. The intended RF EH system's block diagram.

2. Methods / Experimental

A four-sided microstrip patch antenna situated on a concentric circular FR4 substrate with a dielectric constant of $\varepsilon r = 4.4$, a thickness of h = 1.6 mm, and a loss tangent of $\delta = 0.0009$ constitutes the single element that forms the basis of the concentric antenna array design. While Figures 2(b) and 2(c) show the top and rear views of the antenna element, Figure 2(a)

clearly displays the dimensions of the rectangular-shaped patch antenna. The following equations can be used to compute the patch antenna's length (L) and width (W).

$$W = \frac{c_0}{2f_r} \sqrt{\frac{2}{\varepsilon_r + 1}} = \frac{3 \times 10^8}{2 \times 2.45 \times 10^9} \sqrt{\frac{2}{4.4 + 1}}$$
 (1)

$$L = \frac{c_0}{2f_r \sqrt{\varepsilon_{r_{eff}}}} - 2\Delta L \tag{2}$$

$$\Delta L = 0.412(h) \frac{\left(\varepsilon_{r_{eff}} + 0.3\right)\left(\frac{w}{h} + 0.264\right)}{\left(\varepsilon_{r_{eff}} - 0.258\right)\left(\frac{w}{h} + 0.8\right)}$$
(3)

$$\varepsilon_{r_{eff}} = \frac{\varepsilon_{r+1}}{2} + \frac{\varepsilon_{r-1}}{2} \left[1 + 12 \frac{h}{W} \right]^{-1/2} \tag{4}$$

2.1 Simulation Results

Figure 3(a) displays the simulation outcomes for the single antenna element's return loss (S11). The return loss at 2.45 GHz is set up to be -47.51 dB, which is less than -10 dB, making it appropriate for EH from a variety of common wireless systems. Figure 3(b) displays the simulation results for the single antenna element's Voltage Standing Wave Ratio (VSWR), showing that the VSWR value at 2.45 GHz is equal to one.

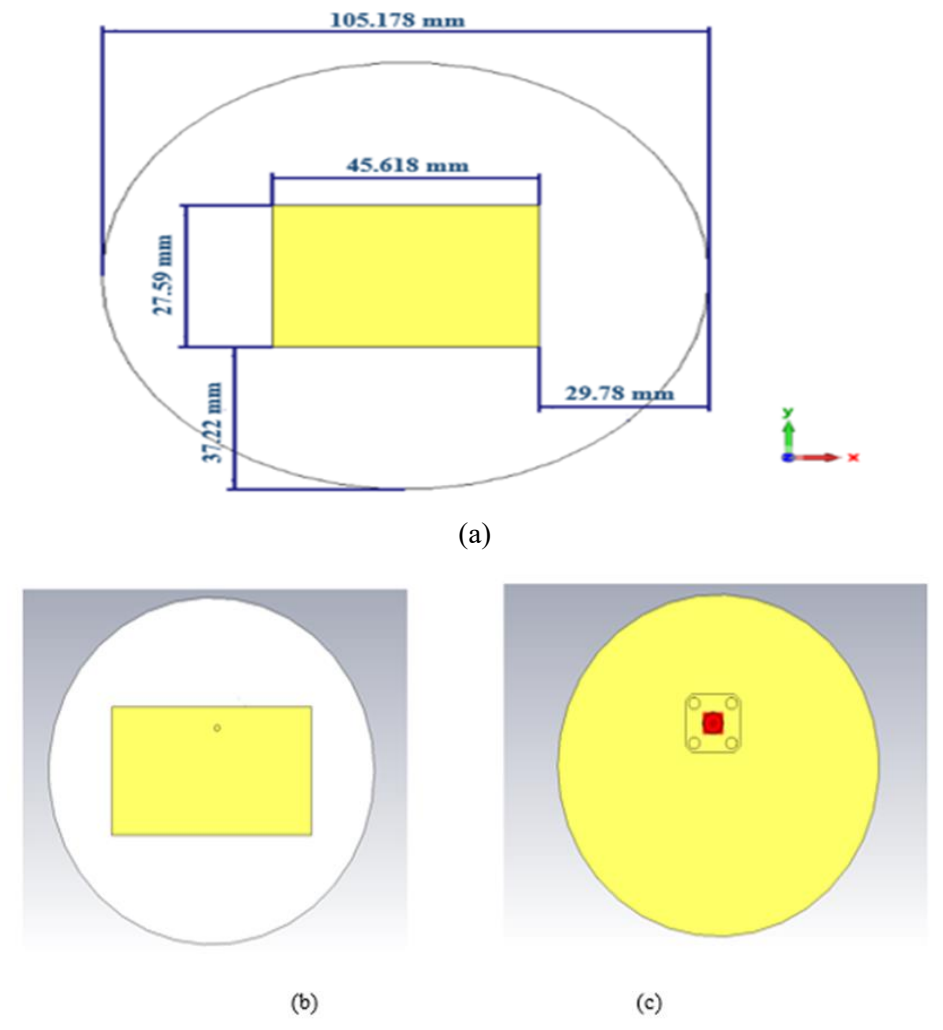


Figure 2. Planned Antenna Structure (a) Dimensions of the planned single element antenna. (b) Top side (c) Bottom side

The detailed simulated radiation pattern at a frequency of 2.45 GHz is presented in an impressive three-dimensional view in Figure 4(a), showcasing various aspects and features. The antenna achieves a gain of 3.89 dBi and maximum directivity of 6.94 dBi, displaying an effective omnidirectional pattern. Simulated radiation patterns in the xz-plane ($\phi = 0^{\circ}$) and yz-plane ($\phi = 90^{\circ}$) are shown in Figures 4(b) and 4(c). Peak radiation occurs at $\theta = 0^{\circ}$ in the yz-plane at 2.45 GHz, highlighting its functionality and reliability for diverse applications.

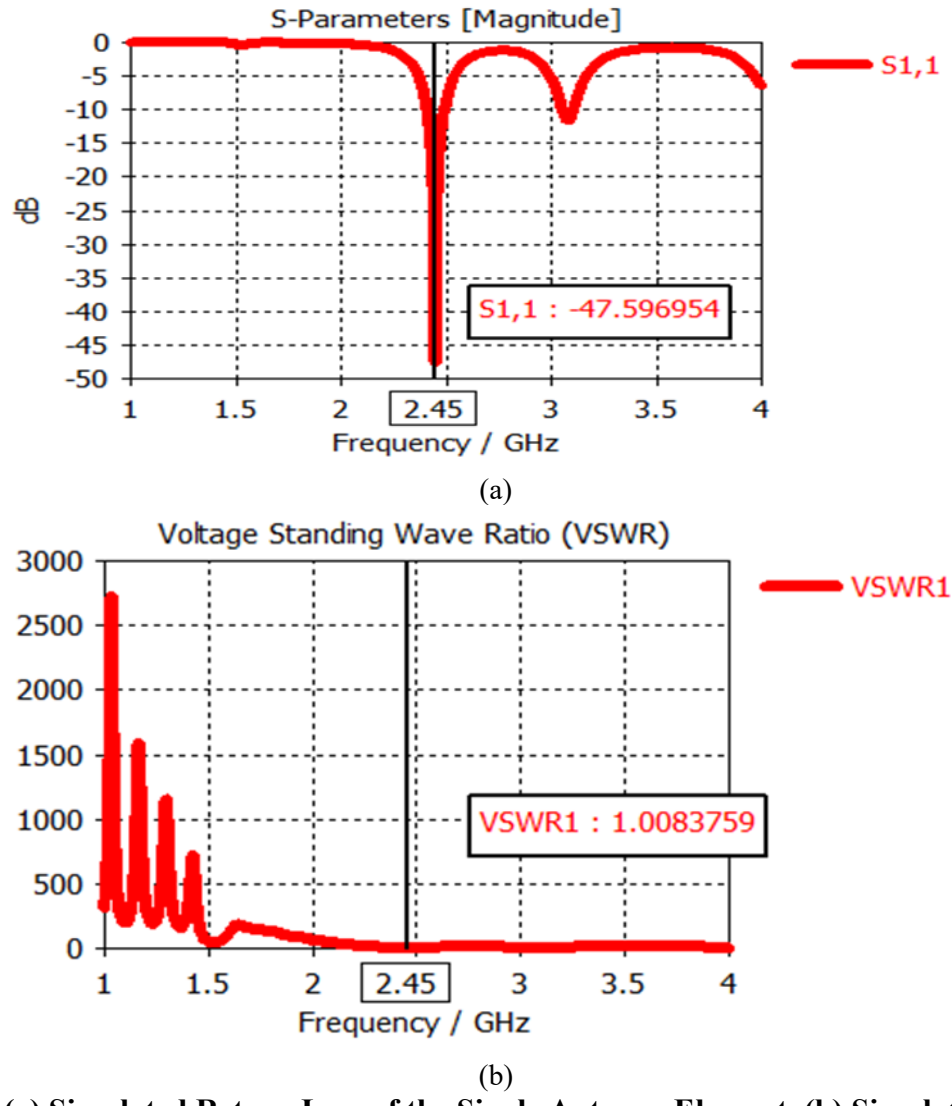


Figure 3. (a) Simulated Return Loss of the Single Antenna Element. (b) Simulated VSWR of the Single Antenna Element.

3. Planned Antenna Array Design

This section plans a microstrip circular antenna array for Electromagnetic Harvesting (EH) applications, using rectangular patch antenna elements arranged on a circular substrate. Figure 5(a) illustrates the front perspective of the antenna array and its dimensions, while Figure 5(b) shows the rear view, enhancing understanding of its design. The optimization of antenna parameters was conducted using CST Microwave Studio, software known for

effective antenna design. Table 1 documents the final measurements of the elements. The main goal was to match the antenna's input impedance to a standard 50 Ω at 2.45 GHz for efficient operation. This design features M=4 rectangular patch elements, each operating at 2.45 GHz, with a gain of 4.05 dBi, all placed on a circular FR4 substrate with a relative permittivity of $\varepsilon r = 4.4$ and a thickness of h = 1.6 mm.

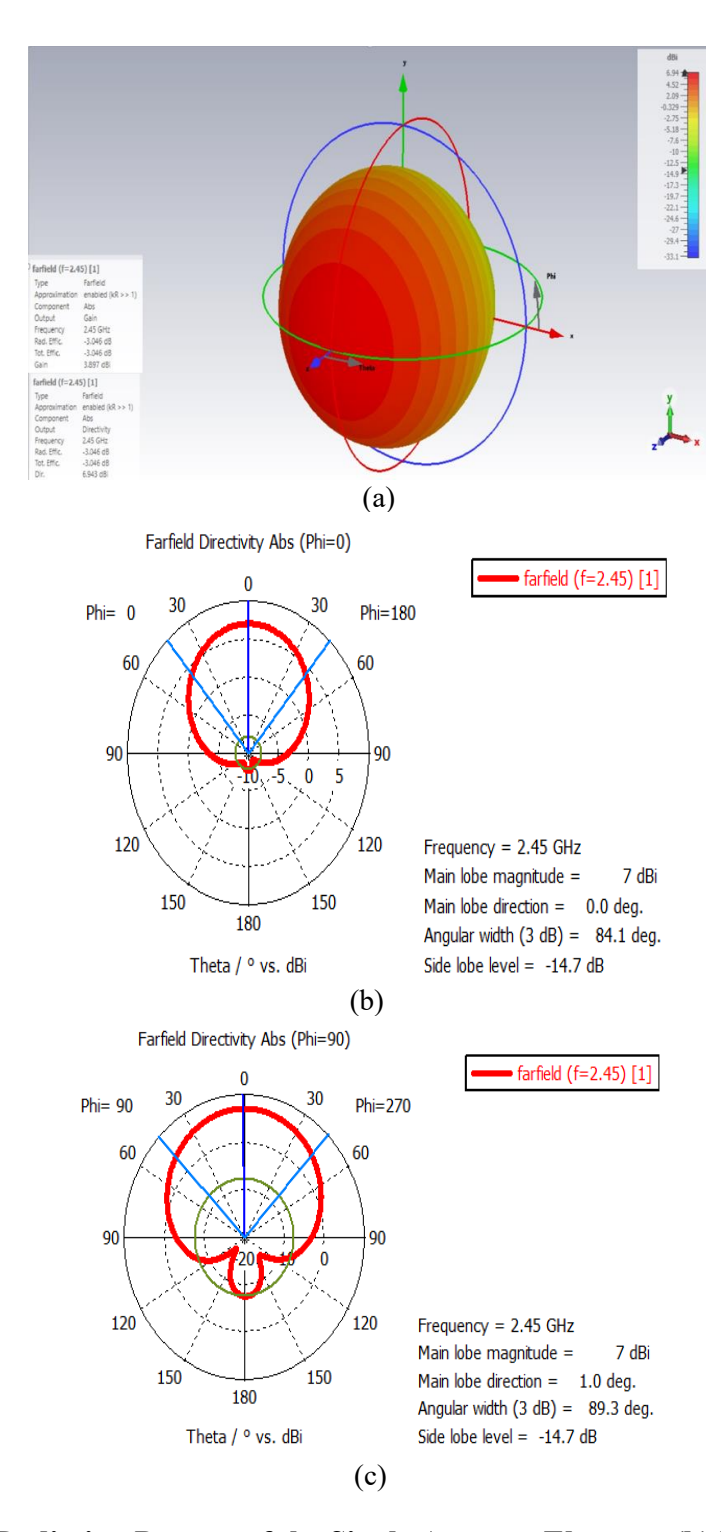


Figure 4. (a) 3-D Radiation Pattern of the Single Antenna Element. (b) E-Plane and (c) H-Plane Radiation Pattern of the Single Antenna Element

Table 1. Antenna dimensions in mm.

Parameter	X	Y	W	L	N	M	R
Dimension (mm)	1.306	9.238	45.618	27.59	60.0304	14.41	97.25

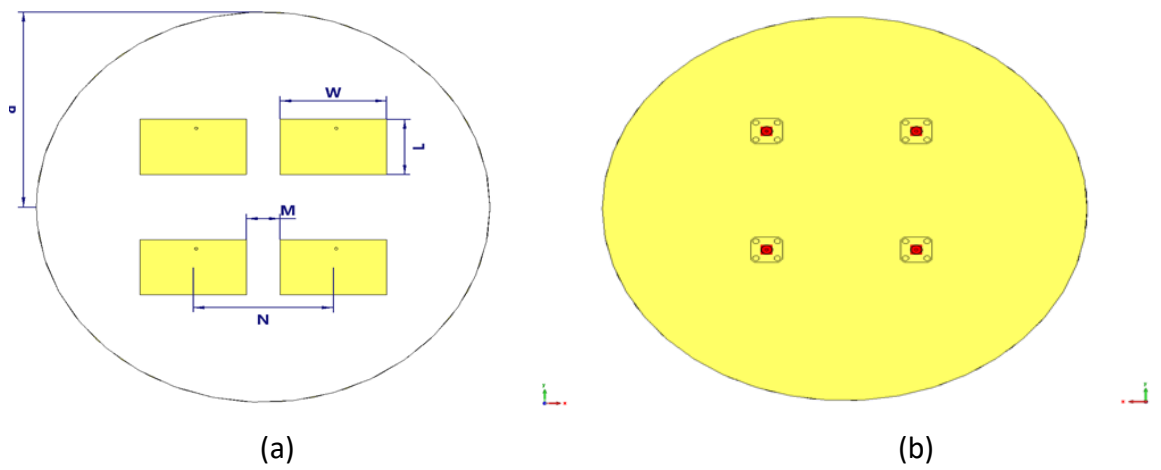


Figure 5. the intended antenna array arranged using the CST microwave studio software. Front side (a) and rear side (b).

The simulation results for the return losses S11, S22, S33, and S44 of the four elements in the antenna array are made known in Figure 6(a), where it is observed that the return losses are below -26.859 dB at 2.45 GHz. This makes it suitable for EH from various standard wireless systems. The simulation results for the Voltage Standing Wave Ratio (VSWR) of the antenna array are presented in Figure 6(b), indicating that the VSWR values at 2.45 GHz are approximately 1.09 for each element of the array. Figure 6(c) illustrates good impedance matching of the antenna elements to a 50 Ω load at the operating frequency $f_0 = 2.45$ GHz. Figure 6(d) shows the simulation results for the total efficiency of the antenna elements, which is around -3.6 dB at $f_0 = 2.45$ GHz. The gain of the individual antenna element is calculated over the frequency range from 2 GHz to 3 GHz, providing a gain of 7.63 dBi at fo = 2.45 GHz. Figures 7(a), 7(b), and 7(c) show the E-plane and H-plane radiation patterns of the proposed antenna array as well as the 3D radiation pattern. The overall gain of the array is approximately 15.8 dBi, and it can be detected that the array's radiation pattern at the operating frequency f = 2.45 GHz exhibits omnidirectional characteristics. Lastly, the simulation results for the surface current distribution of the antenna array are shown in Figure 8.

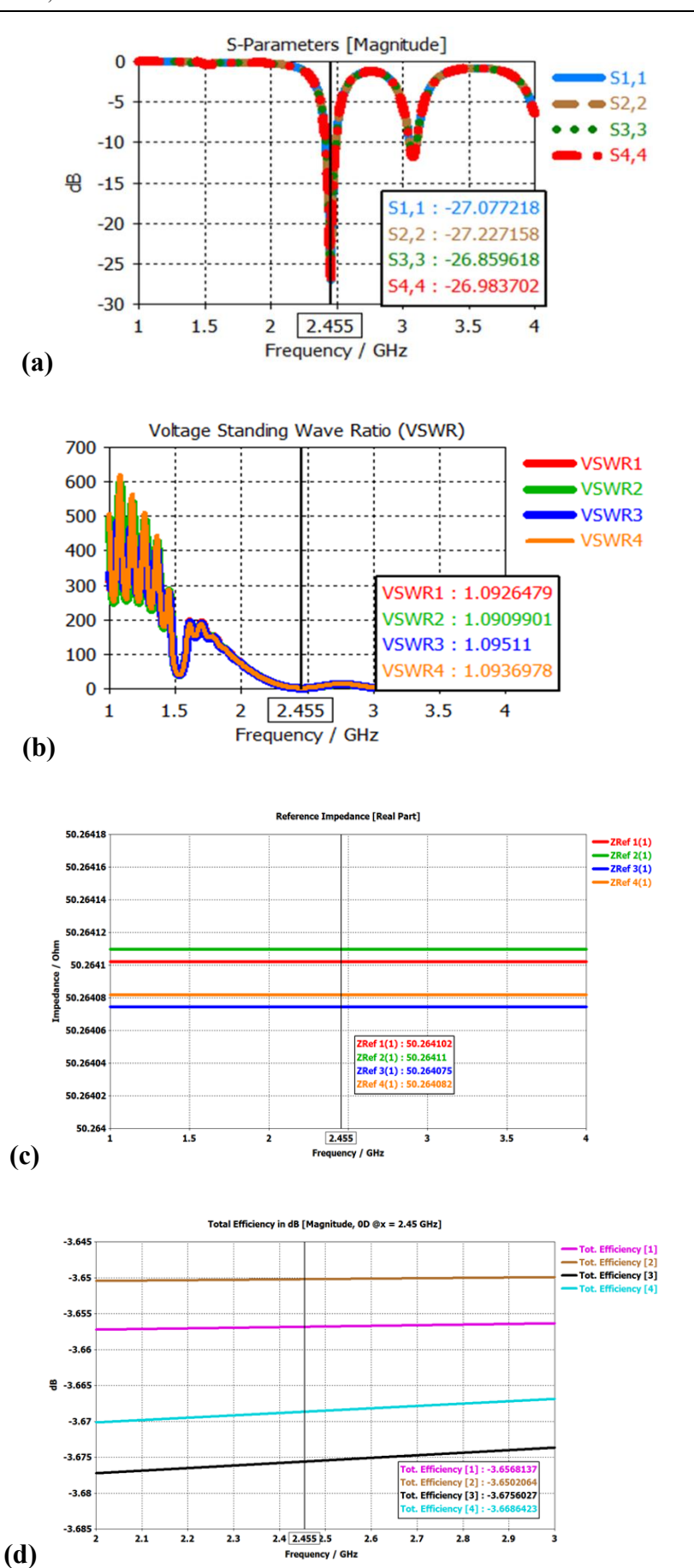


Figure 6. (a) Simulated return losses of the antenna array. (b) Simulated VSWRs of the antenna array. (c) Simulated impedance curves of the antenna array. (d) Total efficiency of the planned antenna array.

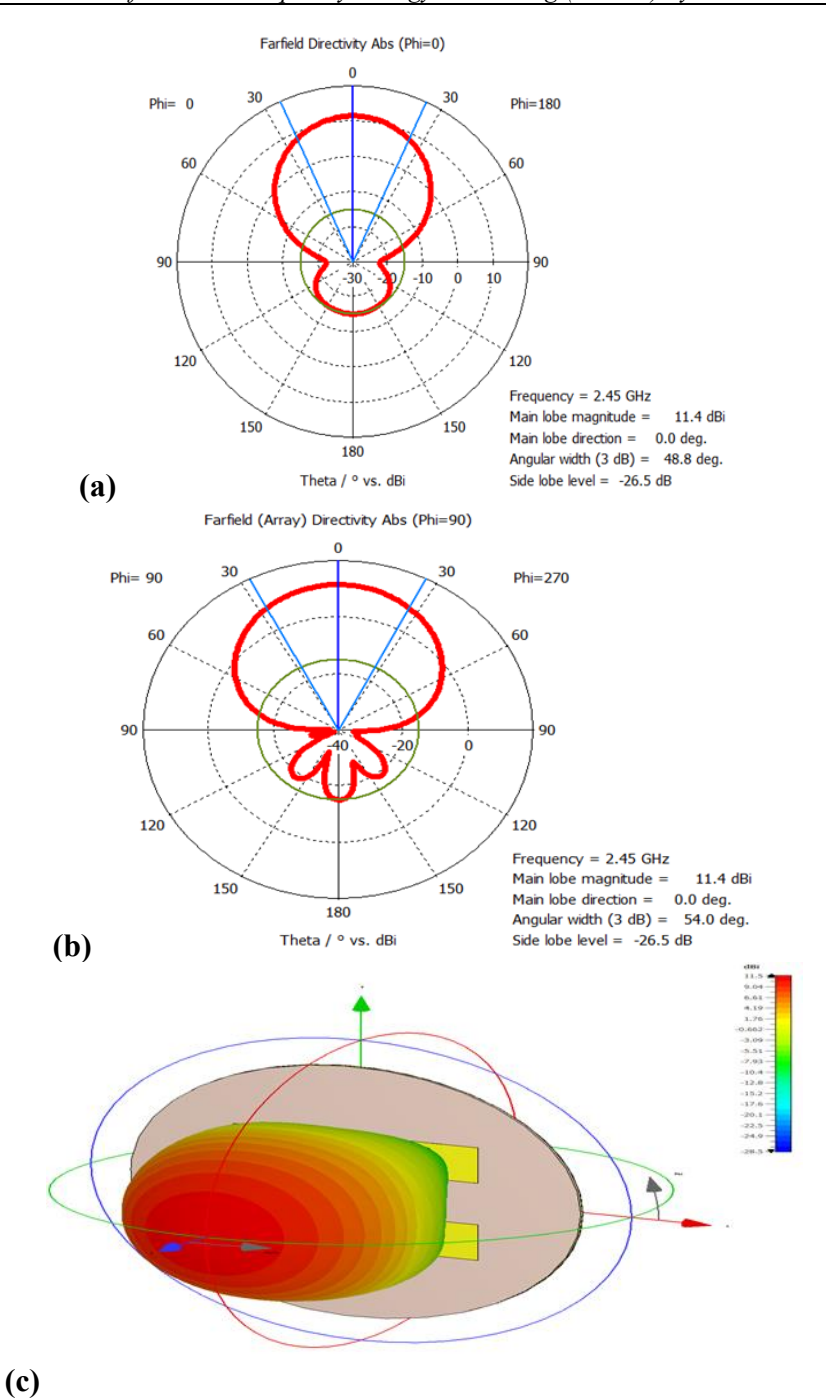


Figure 7. Radiation pattern of the antenna array: (a) E-Plane and (b) H-Plane. (c) 3-D Radiation.

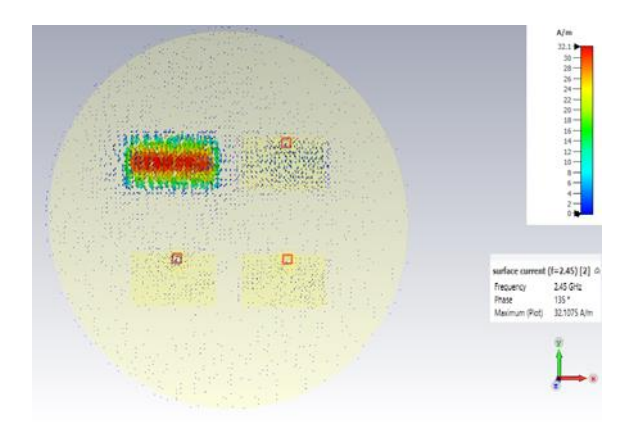


Figure 8. Simulated surface current distribution of the antenna array.

90

3.1 Fabrication Design and Results

The fabricated front and back of the antenna array are presented in Figures 9(a) and 9(b). The reflection coefficients of the antenna array were measured using a Vector Network Analyzer (VNA), as shown in Figure 9(c).

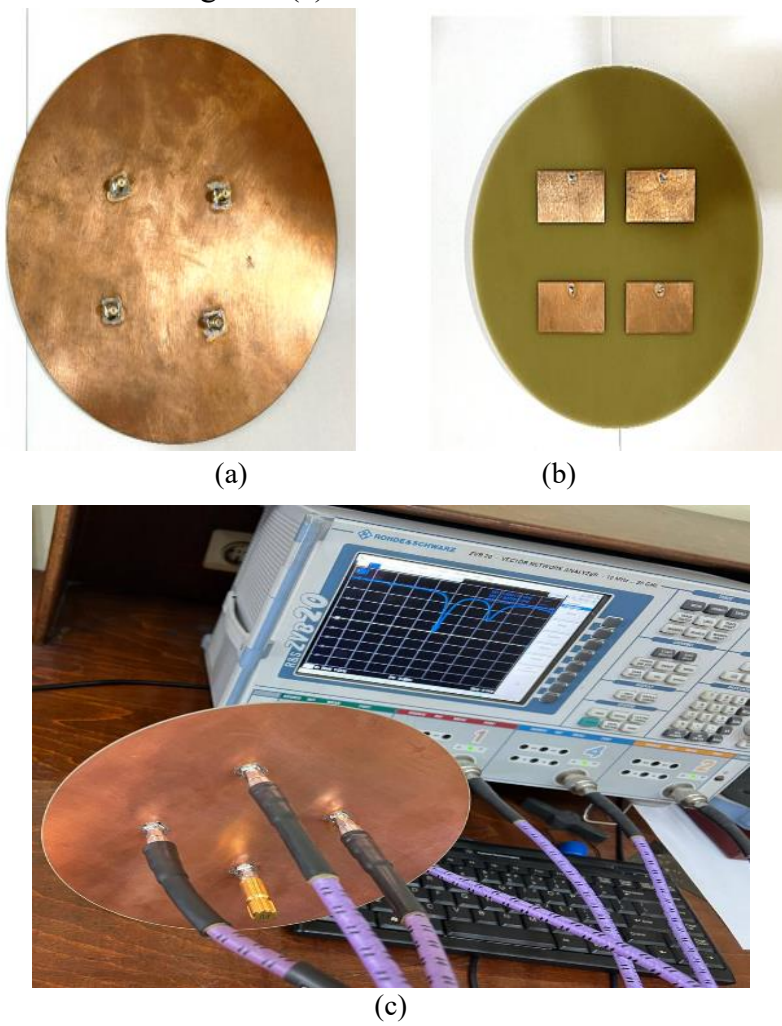


Figure 9. Fabricated Antenna Array. (a) Front side, (b) Back side and (c) Measurement of Reflection Coefficients of Antenna Array by VNA.

Figure 10(a) presents the measured scattering parameters of the constructed antenna array, revealing that the return loss is below -10 dB when compared to the results obtained from CST simulations. The results from the CST simulation exhibit a favorable correlation with the experimental measurements gathered through the VNA. Nonetheless, a discrepancy of 0.04 GHz has been noted between the simulated resonance frequency (fs) and the experimentally determined resonance frequency (fm), which can be attributed to fabrication inaccuracies. At the measured resonance frequency (fm), the reflection coefficient is -22 dB, which is near to the simulated value of -25 dB. Figures 10(b) and 10(c) illustrate the 2D E-plane and H-plane radiation patterns of the antenna array. An observed discrepancy of roughly 0.04 GHz was noted between the resonance frequency obtained from simulations and that determined through measurements of the antenna array. This discrepancy is mainly due to fabrication tolerances, manual soldering, and variations in the dielectric constant of the FR-4 substrate, which are common in practical RF prototyping.

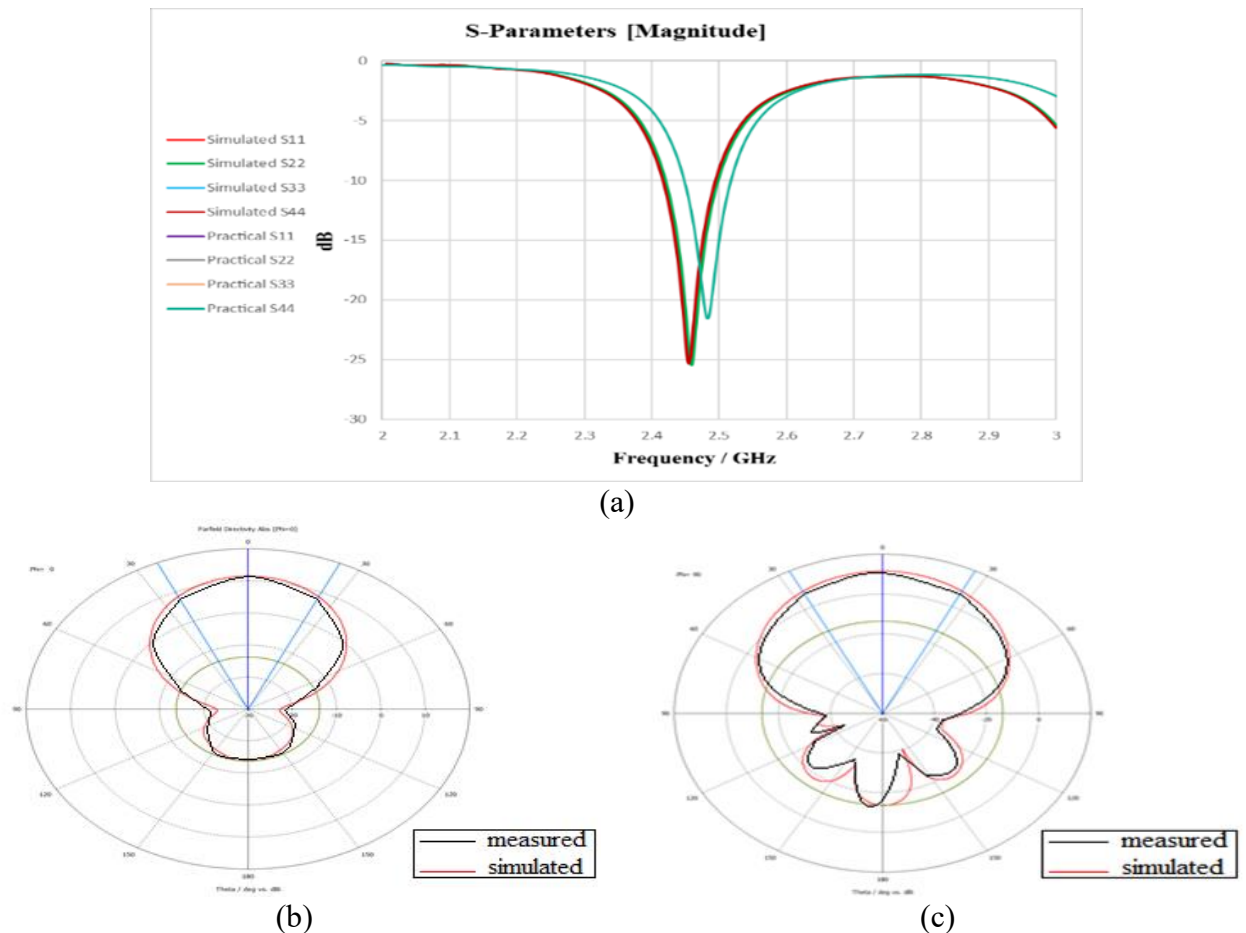


Figure 10. Measured and simulated Parameters of the Antenna Array. (a) scattering parameters, (b) E-plane radiation pattern and (c) H-plane radiation pattern

4. Equal Power Combiner Design

Power dividers (or combiners) are extensively operated in numerous microwave/RF circuits, including antenna array systems. The use of a circular sector multi-port power combiner can be attributed to its beneficial characteristics. A novel quad-port for this sector power combiner is announced as the combining circuit for the antenna array. Stub and inset matching methods are employed to adjust both the amplitude and phase of the signals that enter each branch. This adjustment plays a crucial role in ensuring that the impedances of the branches align effectively with the desired power distribution ratio. Figures 11(a) and 11(b) illustrate the planned antenna array system featuring the circular sector power combiner, which comprises two main components:

- **1.** The antenna array: This is a homogeneously spaced array containing of quad rectangular patch antenna elements.
- 2. The combining network: The circuit in question serves as a multi-port power combiner, facilitating the aggregation of power derived from various receiving elements. The operational framework for the circular sector power combiner is articulated in the equation presented below.

$$f = [A.R^{(B)}]. \varepsilon_r^{(C+D/R)}$$
(5)

Where:

$$A = (182 + 60.6h + 374h^2 - 174h^3) (6)$$

$$B = (-0.952 - 0.432h + 0.159h^2 - 0.00544h^3)$$
 (7)

$$C = (-0.508 + 0.101 h - 0.121h^2 + 0.0383h^3)$$
(8)

$$D = (0.21 - 2.56 h + 0.778h^2 - 0.138h^3)$$
(9)

Where ε_r r is the substrate dielectric constant, h is the substrate thickness in millimetres, and R is the sector radius in millimetres. The envisioned equal four-port power combiner with 50 Ω , SMA connectors is depicted from the front and back in Figure 18. The operation frequency is determined by the sector radius. The power combiner is made using a Rogers RO3010 substrate, which has a height of 1.27 mm and a dielectric constant of ε_r =10.2. At a frequency of f =2.45 GHz, the sector radius obtained by applying the scheme formulation from Eq. (5) is found to be R=24 mm. As shown in Figure 11(c), the power combiner's modified dimensions in millimeters, as determined by the CST Microwave Studio software program, are shown in Table 2.

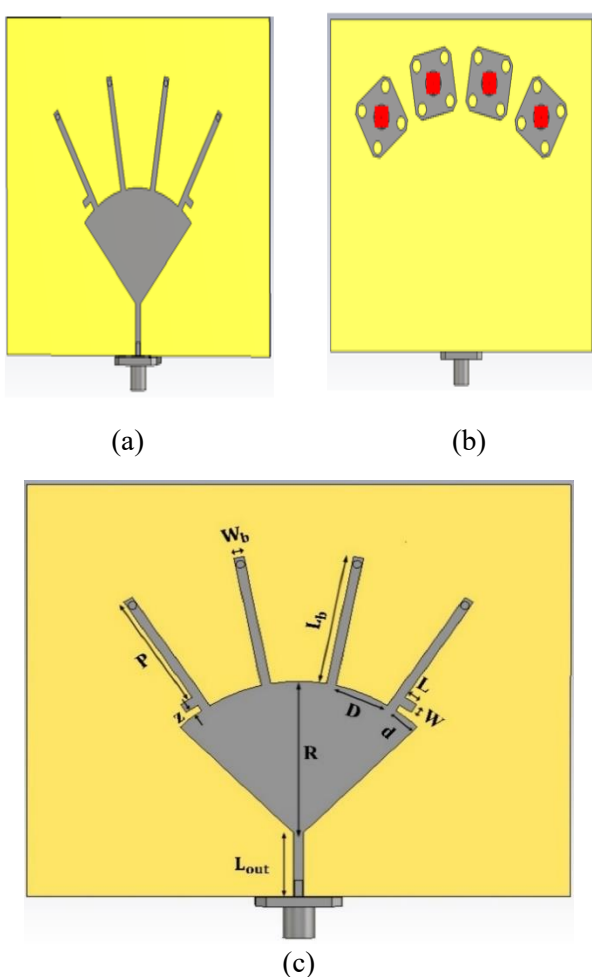


Figure 11. Planned Circular Equal Power Combiner Structure (a) Top View and (b) Bottom View. (c) Parameters of Circular Equal Power Combiner.

4.1 Fabrication Design and Results

Figures 12(a) and 12(b) illustrate the fabrication prototype of a circular equal power combiner. The S-Parameters of the circular equal power combiner were measured using a VNA, as depicted in Figure 12(c). The simulation results for the return loss S11 and transmission coefficients S12, S13, S14, and S15 of the four elements of the circular equal power combiner are presented in Figure 13(a). It can be observed that the return loss S11 is below -10 dB at 2.45 GHz, measuring -32.77 dB, while S12=-7.08, S13=-5.53, S14=-5.53, and S15=-7.08. The simulation results for the impedance of the circular equal power combiner are shown in Figure 13(b), indicating that its value at 2.45 GHz is nearly 49 Ω for each element of the power combiner. The scattering parameters of the fabricated circular equal power combiner, compared to the results from CST simulations, are presented in Figure 13(c). The data reveals a strong correlation between the CST simulation outcomes and the experimental measurements derived from the Vector Network Analyzer (VNA). Nevertheless, a discrepancy of 0.1 GHz is observed between the simulated resonance frequency (fs) and the measured resonance frequency (fm), which can be attributed to inaccuracies in the fabrication process.

Table 2: circular equal power combiner parameters in (mm)

Parameter	Value (mm)	Description
R	24.6	Sector Radius
θ	90°	Sector Apex Angle
W_b	1.46	Input and Output Branches Width
L_b	20.51	Input Branches Length
Lout	10.03	Outer Branch Length
L	2.00	Stub Length
P	18.02	Stub Distance from Top
Z	1.03	Stub Distance from Bottom
W	1.46	Stub Width
D	8.16	Distance b/w Input Branches
d	4.09	Distance b/w Outer Branches and Sector Beginning
$L_{sub} \times W_{sub}$	80 mm × 65 mm	Substrate Dimensions

A frequency shift of roughly 0.1 GHz was noted between the measured and simulated results for the circular equal power combiner. The same fabrication and material variables are responsible for this shift, which can be reduced in subsequent iterations by implementing improved assembly methods and stricter manufacturing tolerances.

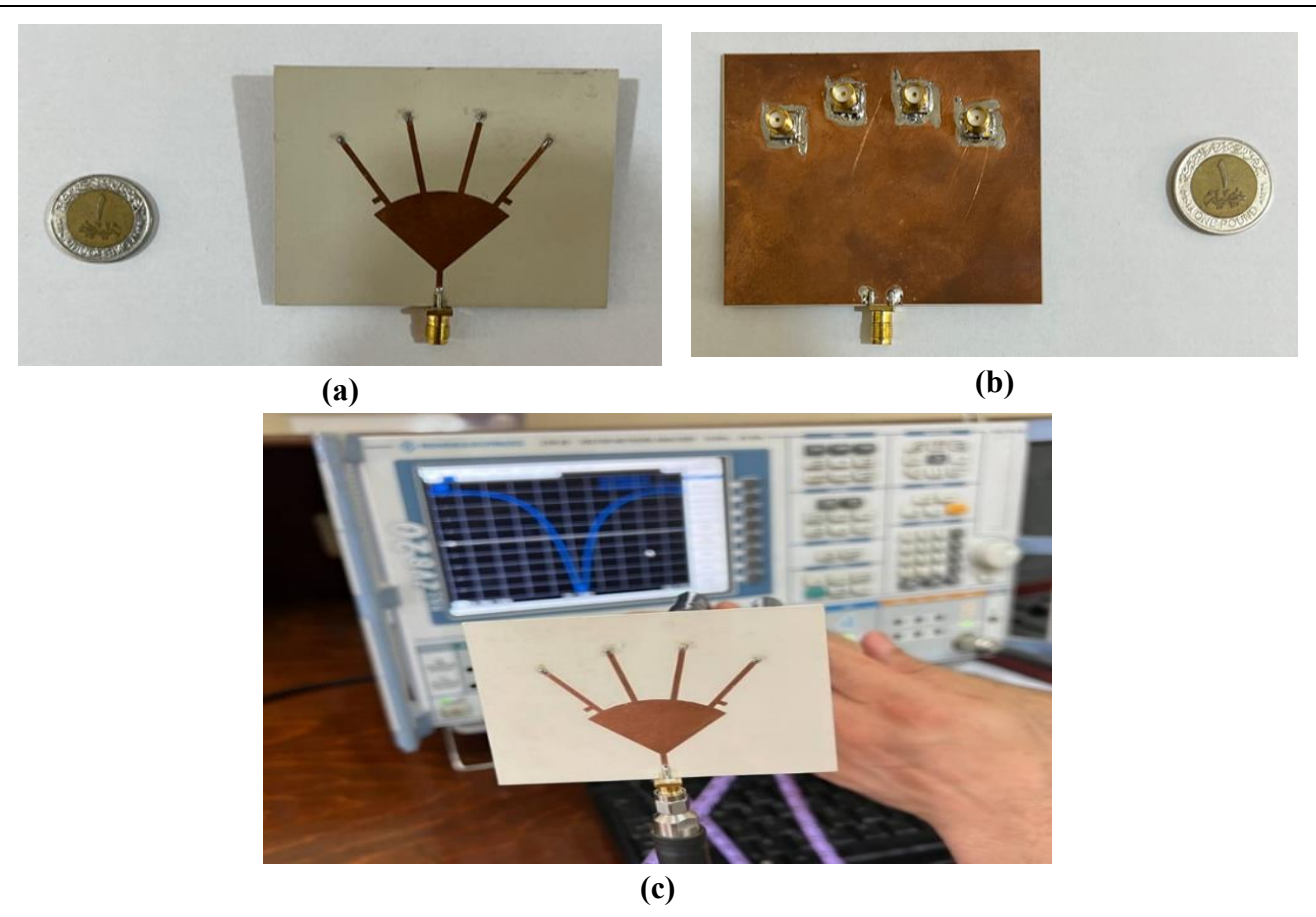


Figure 12. Implementation of Circular Equal Power Combiner Structure (a) Top side, (b) Bottom side and (c) The Fabricated Circular Equal Power Combiner measuring.

5. Design and Implementation of Rectifiers

The third essential part of the RF EH system is the rectifier circuit, which transforms AC voltage into DC voltage. The antenna, matching circuit, and voltage rectifier make up the rectenna circuit, which can capture radio frequency energy. The ratio of the input RF power (Pin).to the output DC power (Pout).is the measure of the efficiency of RF to DC power conversion.

$$\eta_c = \frac{DC \ Output \ Power}{Incident \ RF \ Power} = \frac{V_{out}^2/R_L}{P_{in}} * 100\%$$
 (10)

Where

 η_c is the total efficiency, P_{in} is the incident power (w), R_L is the Load impedance, and V_{out} Output Voltage (V).

After connecting the planned rectifier to the antenna array with the circular equal power combiner, the output voltage is measured 250 mV when the antenna array receives 1.30 mW from Wi-Fi. Thus, the values can be entered into equation (10) to determine the overall efficiency. After performing the calculation, the efficiency was found to be 24.03% for a load resistance of 200 Ω

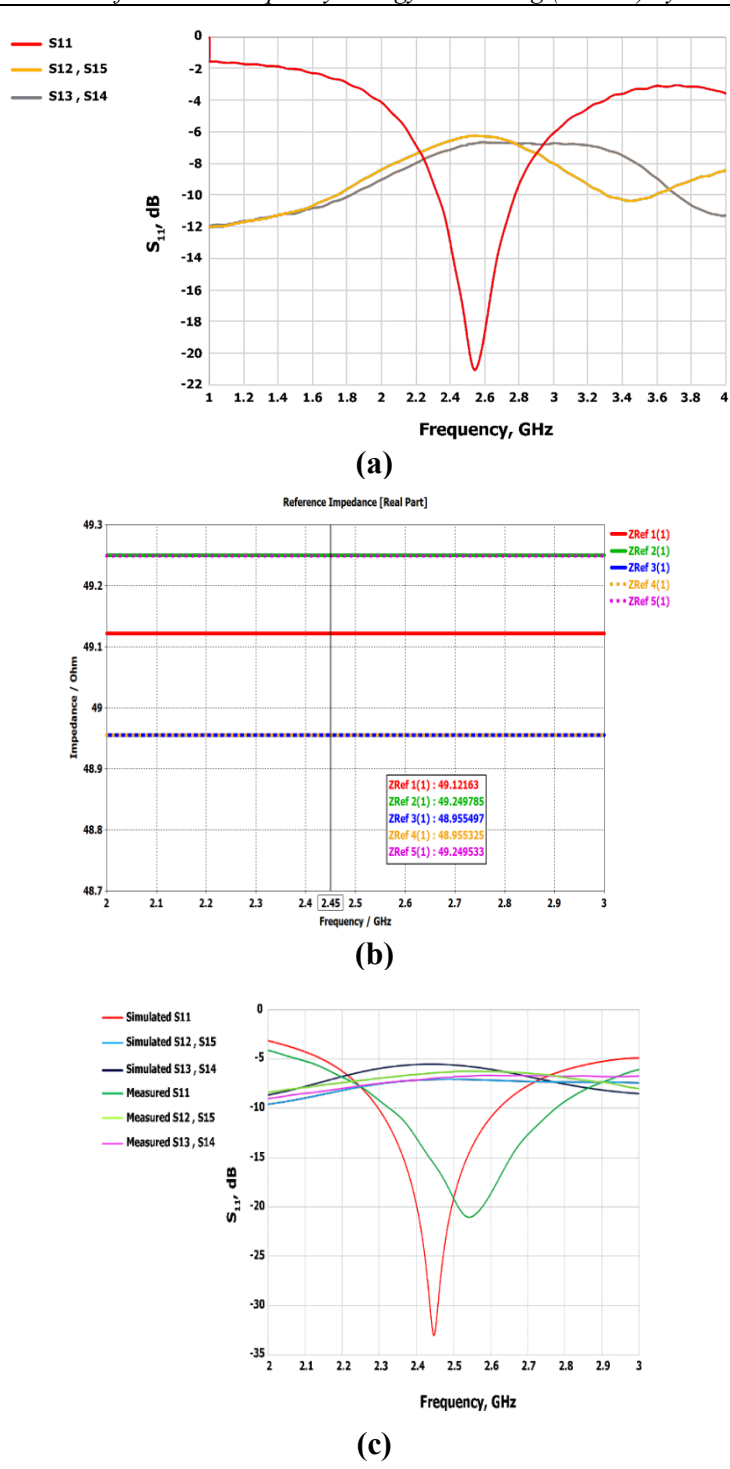


Figure 13. (a) Measured Scattering Coefficients of Fabricated Circular Equal Power Combiner. (b) Simulated Impedance Curve of Circular Equal Power Combiner. And Relationship Among the Measured Scattering Parameters of the Fabricated circular equal power combiner and the CST Simulation Outcomes.

5.1 Determine input impedance using circuit simulation

The modeling and analysis depicted in Figure 14 can be conducted through simulations to approximate the results expected from the real implementation of the rectifier. A simulation tool such as Advanced Design Systems (ADS) or similar software can be utilized. ADS allows for SPICE simulations comparable to LT Spice and other SPICE software and offers the capability to create custom component libraries in addition to using predefined

components. The circuit performance and load resistance can be assessed using ADS through Harmonic Balance simulation, a frequency domain analysis technique for simulating distortion in nonlinear circuits and systems, which is applicable for analog RF and microwave circuits. This simulation method provides frequency domain voltages and currents, enabling direct calculation of the steady-state spectral content of these voltages or currents within the circuit. Another approach to simulate the circuit and ascertain the input impedance of the diode is through S-Parameters simulation, which computes the S-Parameter properties necessary for calculating the reflection coefficient and subsequently the input impedance of the diode, treated as a load in this context. To ascertain the input impedance via circuit simulation, the selected diode must be incorporated into the ADS library, which can be done using the sub-circuit feature. The diode package 1SS351 from ON Semiconductor was chosen due to its close matching to the diode HSMS2852 used in the research reviewed papers; however, it is worth noting that the latter is now an obsolete component.

By utilizing the data provided by the manufacturer, as illustrated in Figures 15(a) and 15(b), the diode model is constructed in ADS to simulate its behavior and compute the input impedance, which is essential for creating the matching circuit. Figure 15(b) demonstrates the implementation of the diode in ADS. Once the diode is incorporated into ADS, simple circuits have been designed and perform an S-Parameter simulation to obtain the reflection coefficient (S11). From this reflection coefficient, the load impedance ZL calculated, knowing that $Z0=50\,\Omega$.

$$S_{11}|_{db} = -20\log(\Gamma), \ \Gamma = \frac{Z_L - Z_0}{Z_L + Z_0}$$
 (11)

Figures 16(a) and 16(b) illustrate the circuit and its simulation results, respectively. The normalized input and output reflection coefficients are given as $Z_{i_normalized}$ =0.215-j0.451 Ω and $Z_{o_normalized}$ =0.620-j1.504 Ω . Knowing that Z_0 =50 Ω , the input impedance is Z_{in} =10.75-j22.55 Ω . This impedance value needs to be matched using any suitable method. The results provided pertain to an unmatched diode, which can function as a half-wave rectifier.

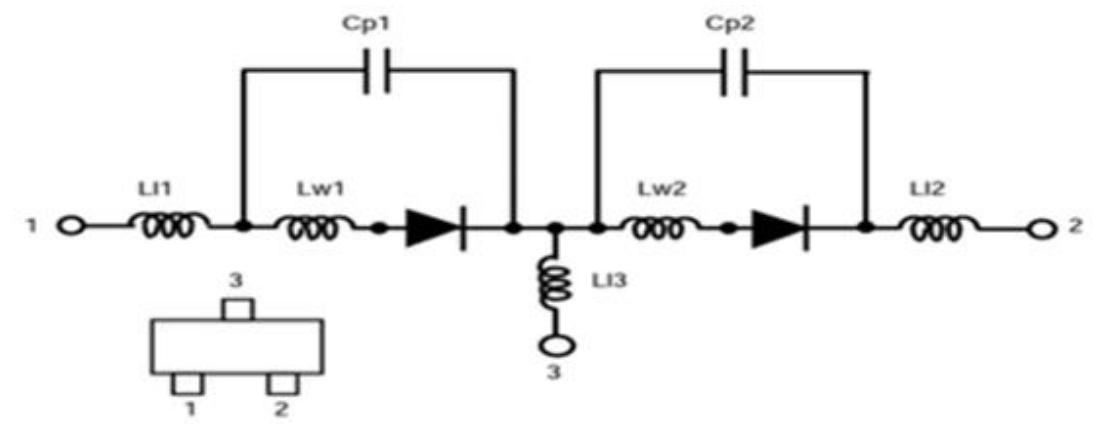


Figure 14. 1SS351 Diode SOT-23 Package Equivalent Circuit.

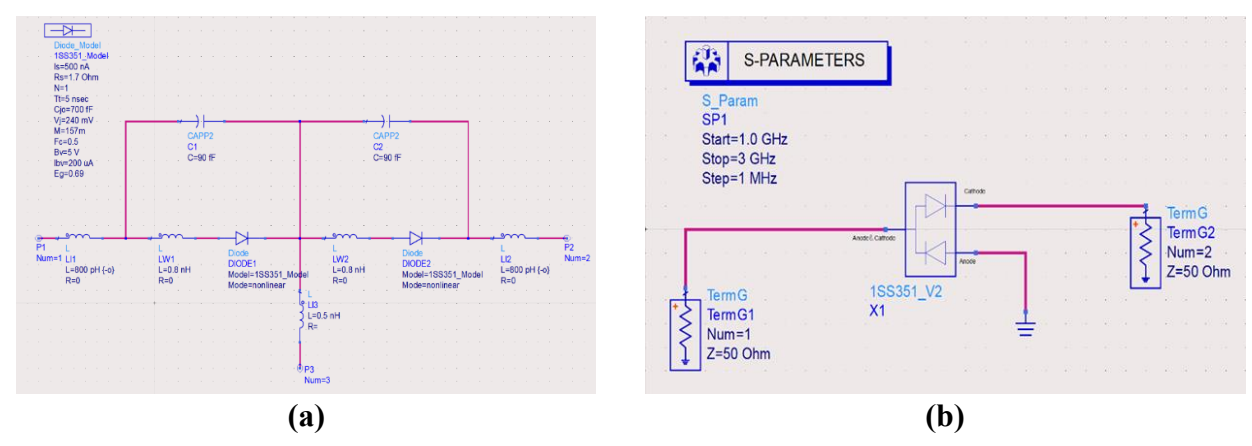
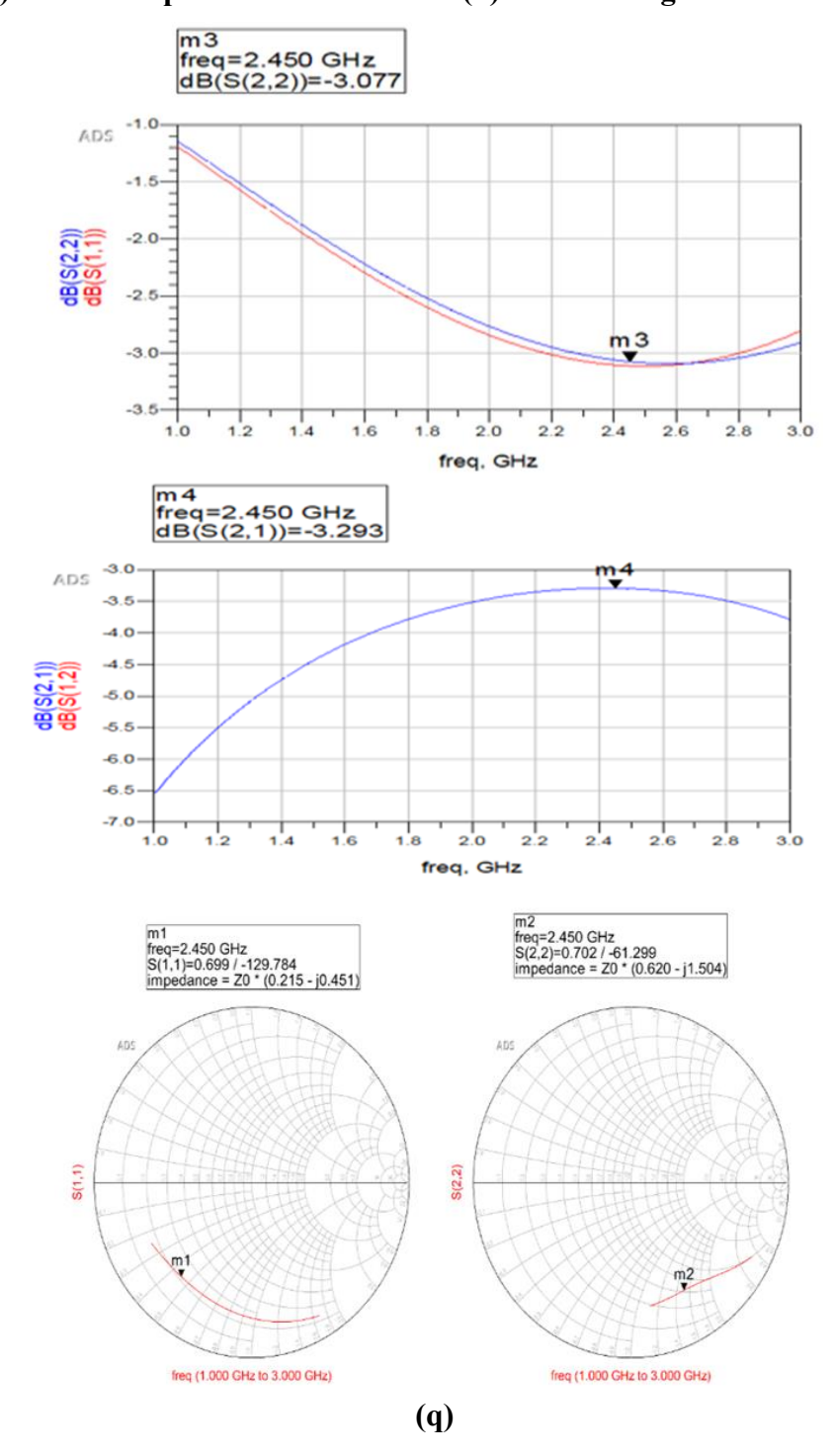


Figure 15. (a) 1SS351 Implementation in ADS. (b) Circuit Diagram for Unmatched Diode.



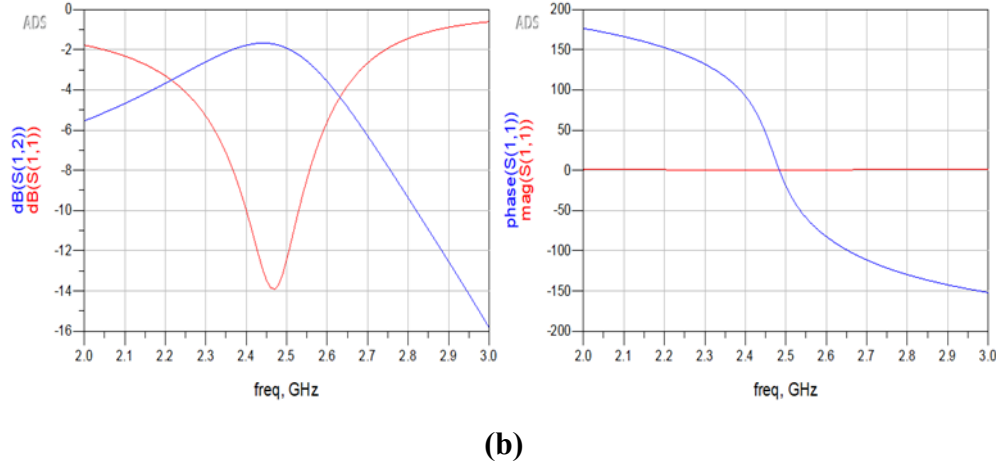


Figure 16. (a) S-Parameter Results for Unmatched Diode. (b) S-Parameter for Matched Half-Wave Rectifier using Microstrip Lines

6. Rectifier Matching

6.1 Half-Wave Rectifier Matching

In this section, matching techniques for half-wave and full-wave rectifiers utilizing Smith charts, lumped elements, and microstrip lines will be explored. The objective of the matching process is to set the real part of Z_{in} to 50 Ω while adjusting the imaginary part accordingly. Figure 17(a) illustrates the matched half-wave rectifier using microstrip lines, and Figure 17(b) presents the S-parameter results for the matched half-wave rectifier with these microstrip lines.

6.2 Full-Wave Rectifier Matching

In order to accomplish Full wave Rectifier matching, it is essential to ascertain the input impedance, employing the same method as before. The matching process for the full-wave rectifier is categorized into two parts: the results for the unmatched full-wave rectifier and those for the matched full-wave rectifier.

A. Unmatched Full-Wave Results

Figure 18(a) illustrates the circuit for the unmatched full-wave rectifier. As exposed in Figure 18(b), the normalized input and output reflection coefficients are $Z_{i_normalized}$ =0.037-j0.835 Ω . Given that Z_o =50 Ω , the resulting input impedance is Z_{in} =1.85-j41.75 Ω . It is significant to observe that the use of a full bridge meaningfully raises the imaginary component of the impedance due to the characteristics of the RF model for diodes, which considerably increases the imaginary part. Consequently, it may be more practical to utilize a half-wave rectifier instead of a full-wave rectifier, as the increase in the non-real component could negatively impact overall efficiency without proper matching.

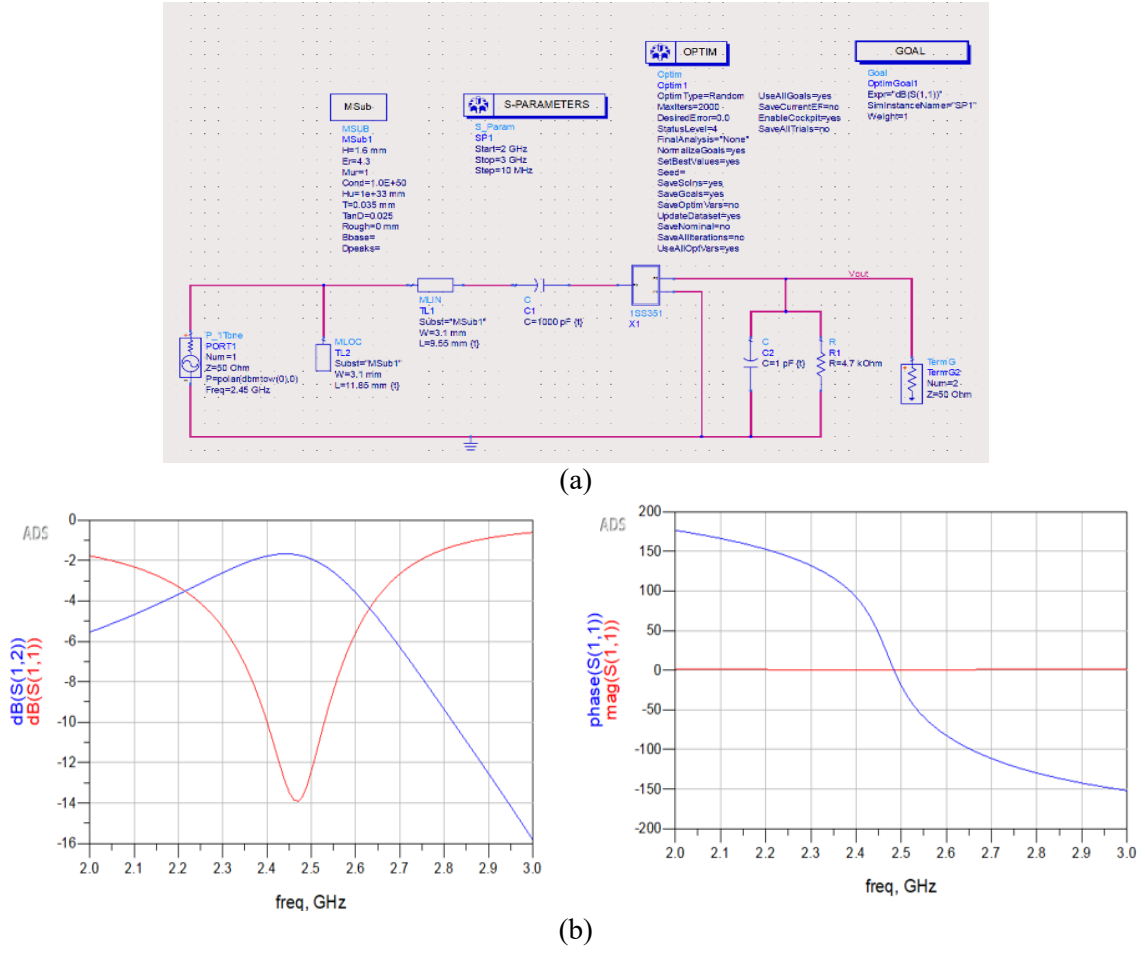


Figure 17. (a) Matched Half-Wave Rectifier using Microstrip Lines. (b) S-Parameter for Matched Half-Wave Rectifier using Microstrip Lines.

B. Matching Full-Wave Results

B.1 Matching Using Lumped Elements

Figure 19(a) depicts the matching circuit for the full-wave rectifier using lumped elements. Figure 19(b) presents the planned results; however, this design is impractical due to the requirement for components valued at 53 Ω and 2.7 nH, both of which are difficult to source off the shelf. Consequently, the realization of this design is not feasible.

B.2 Matching Using Microstrip Lines

Figure 20(a) illustrates the microstrip line matching circuit for the full-wave rectifier. The results presented in Figure 20(b) are generally lower than those achieved with lumped element matching; however, this approach is easier to implement, particularly if the manufacturer can produce PCBs with a precision of 0.001 mm. The fabrication of the employed diode is displayed in Figure 21(a), using an FR4 epoxy substrate.

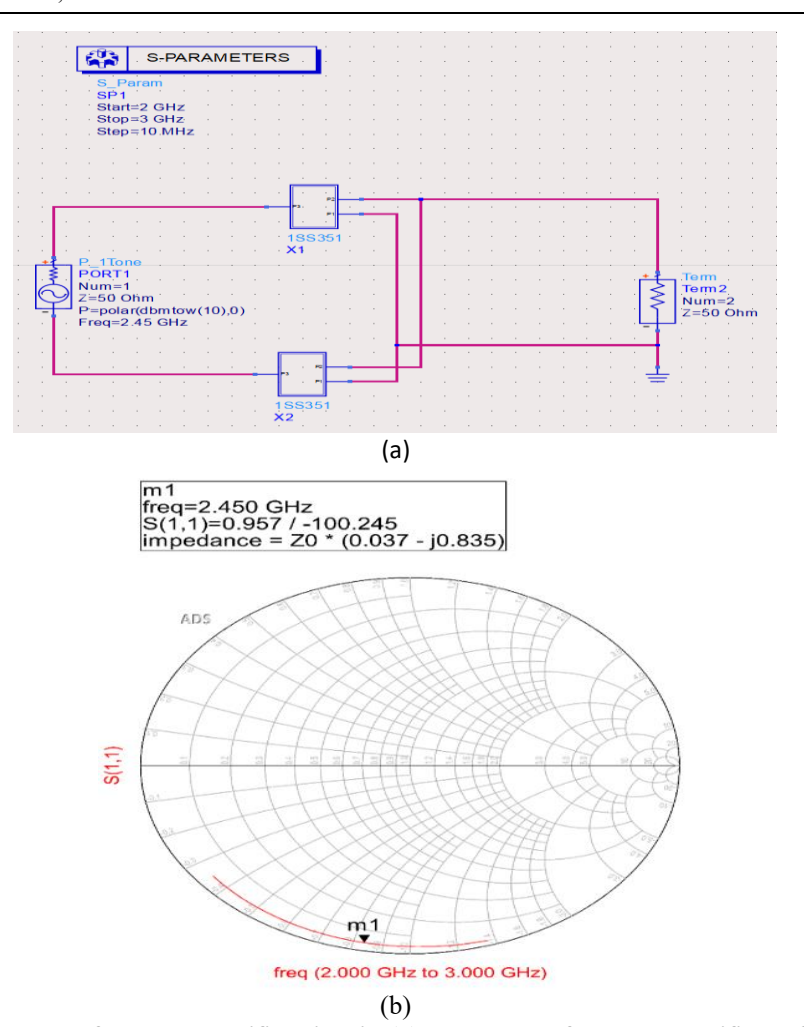


Figure 18. (a) Unmatched full-wave rectifier circuit. (b)Unmatched full-wave rectifier reflection coefficient

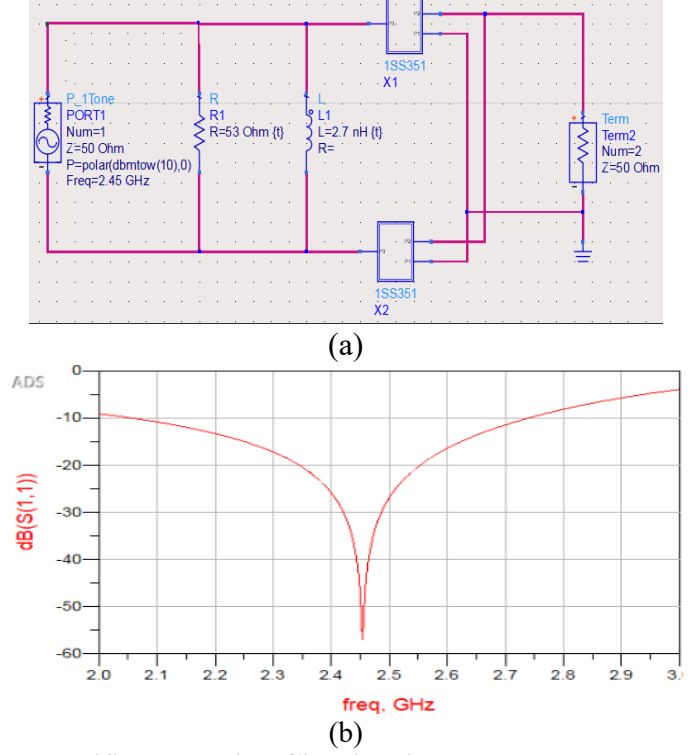


Figure 19. (a) Full-Wave Rectifier Matching Circuit using Lumped Elements. (b) Full-wave rectifier matching S₁₁ using lumped elements

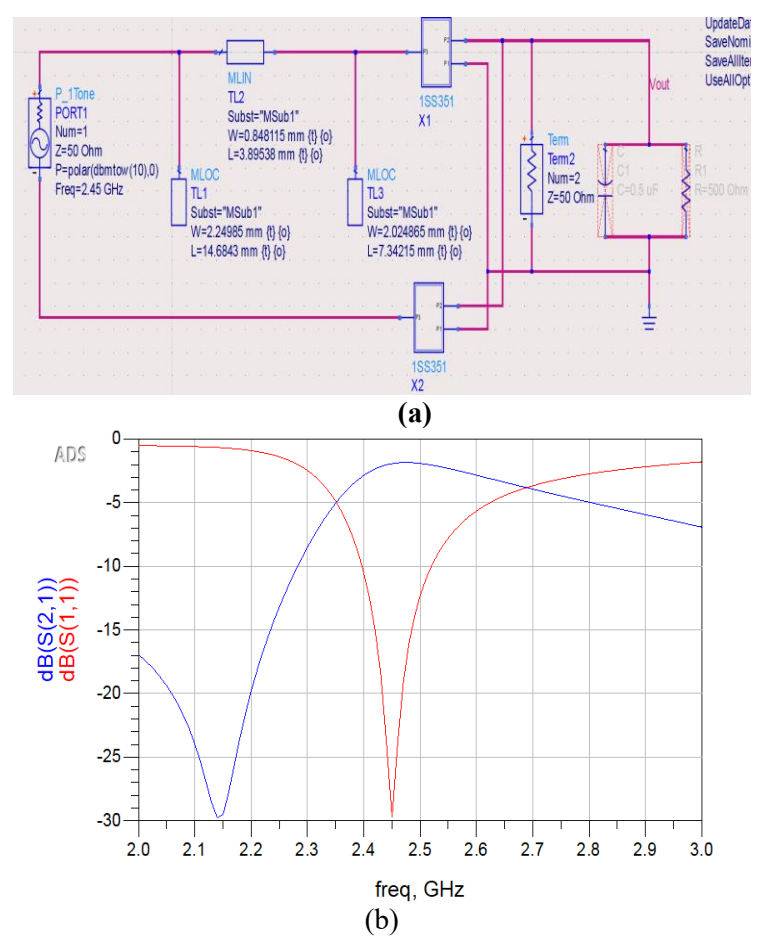
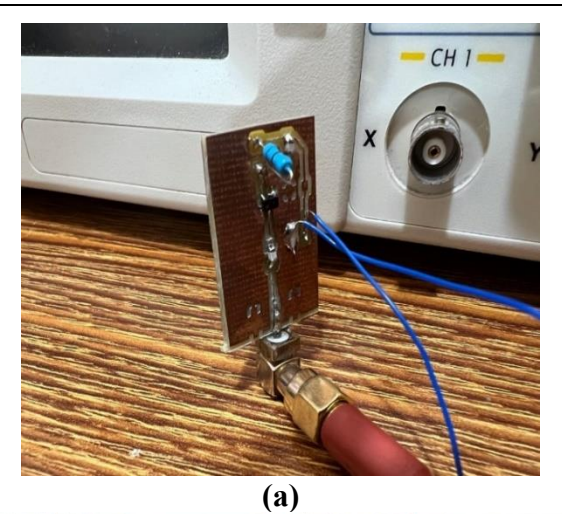


Figure 20. (a) Microstrip Line Matching for Full-Wave Rectifier Circuit. (b) Microstrip Line Matching S-Parameters

Implementation of (RF-EH) system

The implementation of a RF harvesting device involves capturing ambient RF signals to produce electrical power. Figure 21(b) illustrates the device's implementation, which naturally covers an antenna, a rectifier, and an energy storage unit. The antenna gathers the RF signals present in the environment and changes them into alternating current (AC) signals. Subsequently, the rectifier transforms these AC signals into direct current (DC) signals, which are better suited for charging batteries or powering electronic devices. The energy storage unit retains the generated electrical power for future use. This approach enables the utilization of otherwise wasted energy from various sources, including Wi-Fi routers, cell phone towers, and television broadcasts. By efficiently capturing and converting these RF signals into usable electricity, this technology provides a sustainable and eco-friendly solution for powering little-power electronic devices while decreasing dependence on traditional power sources. Table 3 presents a comparison of the enhanced RF-EH system with prior research in the RF-EH domain. The assessment highlights essential features such as size, resonance frequency, output voltage and power, rectifier type, and power conversion efficiency (PCE).



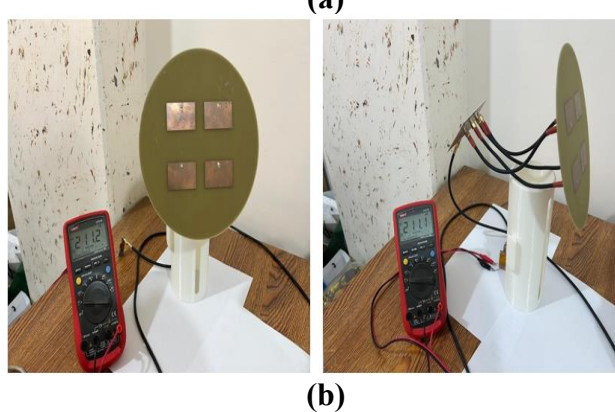


Figure 21 (a) Fabrication of Planned Rectifier. (b) Implementation of RFEH based on planned Antenna array combined with power combiner

Table 3 comparison of the enhanced RF-EH system with prior research in the RF-EH domain

	Antenna / Rectifier (mm × mm)	frequency (MHz)	Matching network	Rectifier stages	Substrate	PCE (%) @ input power (dBm)
[44]	53×43.4 / 13.15×8.23	2437	Transmission line stubs	Multiple	PTFE	52.5 @ 7 (Meas.)
[45]	28.5×28 / NA	2400	Open-circuit stub	Seven	FR-4	18.6 @ -50 (Meas.)
[46]	27.5×25.90 / 14×27.5	2400	Transmission line stubs	Two	Rogers TMM10	47.7 @ 11 (Meas.)
[47]	89 × 89 / 55×20	915	N/A	Five	Polymer	20 @ 0 (Meas.)
[48]	53×43.5 / 22.07×26.2	2452	Transmission line stubs	Single	PTFE + FR- 4	33.8 @ 5 (Meas.)
[49]	NA	915	LC-based	Three	CMOS	25 @ 1 (Meas.)
[50]	110×60 / 70×50	915	Short circuit stub	Single	FR-4	25 @ 0 (Meas.)
[51]	54.5×48 / 76.2×38.1	2450	LC-based	Two	FR-4	64 @ 0 (Meas.)
Planned Work	97.25 × 97.25 / 80 × 65	2450	LC-based	Single	Rogers RO3010 + FR-4	24.03 @ 1.3 (Sim. & Meas.)

The (RF-EH) system metrics and performance comparison are summarized in Table 3, the system demonstrates a maximum PCE of 24.03% at Pin ≈ 1.3 dBm, realized using a singlestage single-diode compact rectifier built on a low-cost hybrid substrate (Rogers RO3010 + FR-4). Compared with prior studies, the achieved PCE is lower than the maximum PCE of 52.5% reported in [44] and 64% in [51]. This may be primarily because the rectifiers developed in those studies were multi-stage or more complex structures. On the other hand, the performance is comparable to or even surpasses other multi-stage rectifiers built on lowcost substrates, such as 18.6% [45], 20% [47], and 25% [50] that were developed earlier. Furthermore, the operate in the ambient Wi-Fi band 2.45 GHz, where the available ambient power level is significantly lower than the high-efficiency rectifiers in the 915 MHz ISM band. The high PCE of 24.03% is achieved over the realistic input power level for the ambient Wi-Fi environment. Thus, the RF-EH system demonstrates an acceptable trade-off among PCE, compactness, and ease of fabrication and assembly, manifesting the feasibility of the proposed approach. In order to provide a clearer view of the overall system performance, the Power Conversion Efficiency (PCE) variation with input RF power has been investigated through simulation on ADS software. The performance data including input power (Pin), output DC voltage (Vdc), output power (Pout), and PCE are summarized in Table 4, while the overall PCE trend is shown in Figure 22.

Table 4: Simulation data of the proposed RF-EH system showing input power (Pin), DC output voltage (Vdc), output power (Pout), and PCE values (RL = 200Ω).

Pin_	PCE_	Vdc_V Pout_mW (simulated)			
dBm	percent	(simulated)		(simulated)	
-40	0	0	0	0	
-30	0	≈0	≈0	≈0	
-25	0	≈0	≈0	≈0	
-20	0	≈0	≈0	≈0	
-15	0	≈0	≈0	≈0	
-12	0	≈0	≈0	≈0	
-10	≈0	≈0	≈0	≈0	
-8	0.03	≈0	≈0	0.03	
-6	0.37	0.01	≈0	0.37	
-4	2.78	0.05	0.01	2.78	
-2	10.74	0.12	0.07	10.74	
0	21.61	0.21	0.22	21.61	
0.5	23.24	0.23	0.26	23.24	
1	23.99	0.25	0.3	23.99	
1.14	24.03	0.25	0.31	24.03	
1.5	23.78	0.26	0.34	23.78	
2	22.62	0.27	0.36	22.62	
3	18.12	0.27	0.36	18.12	
5	7.12	0.21	0.23	7.12	
8	0.52	0.08	0.03	0.52	
10	0.04	0.03	≈0	0.04	

104

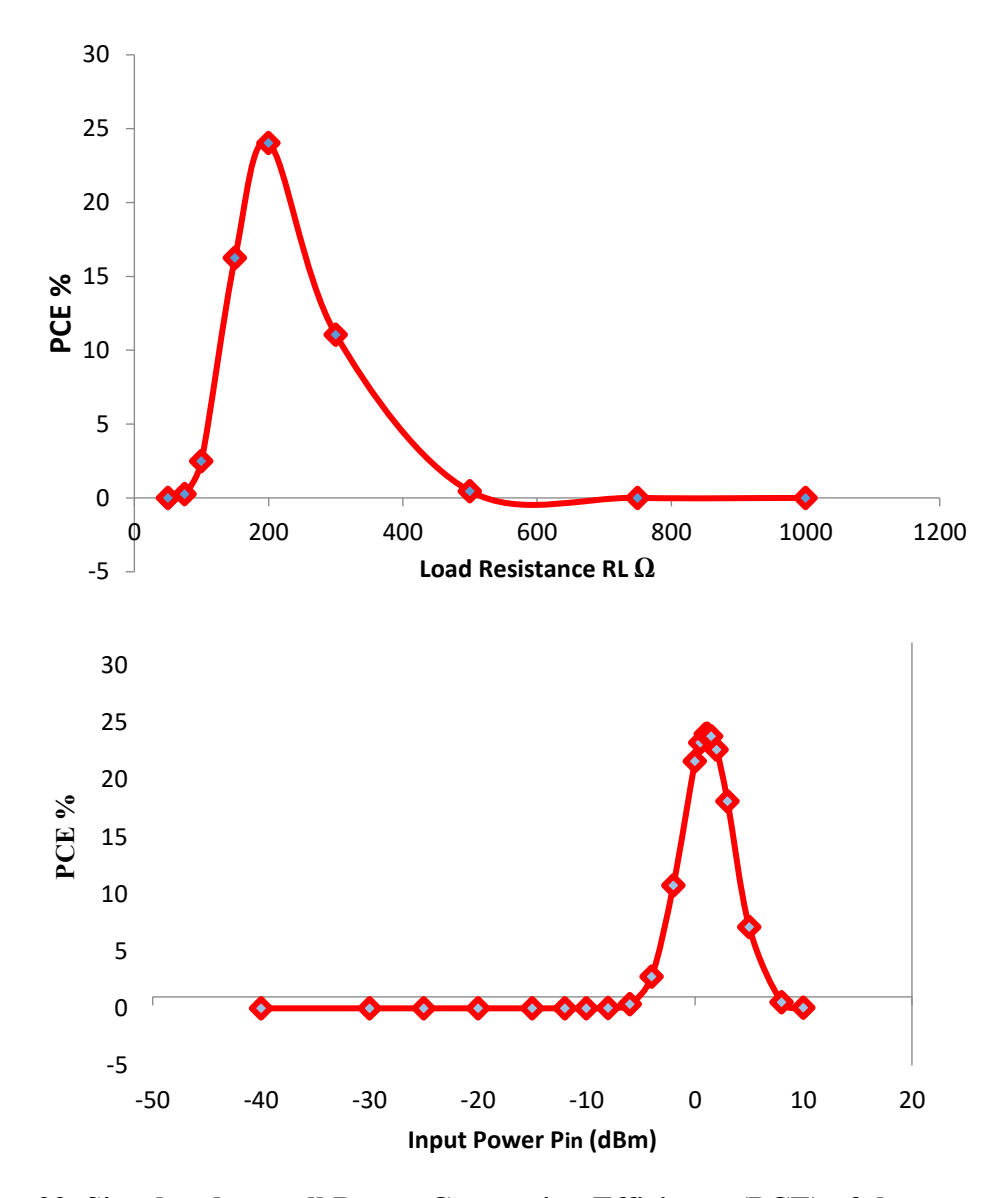


Figure 22. Simulated overall Power Conversion Efficiency (PCE) of the proposed RF-EH system as a function of input RF power

It can be observed from Table 4 that the system achieves a maximum PCE of 24.03% at an input power of 1.14 dBm, corresponding to a DC output voltage of approximately 0.25 V and an output power of 0.31 mW. At very low input powers, the efficiency is limited by the diode threshold voltage, while at higher powers, nonlinear diode behavior and mismatch effects reduce the PCE. As shown in Figure 22, the PCE follows the expected trend, increasing with input power until it reaches a maximum at 1.14 dBm and then decreasing gradually for higher input powers. This trend is consistent with typical rectifier-based RF energy harvesting systems and confirms the validity of the proposed design. To further investigate the system performance, variation of PCE with respect to RL was also studied at Pin \approx 1.3dBm. Shown in Fig. 23 is the simulated PCE as a function of RL from 50Ω to $1k\Omega$. The optimal matching load was found to be RL = 200Ω that gives the maximum PCE of 24.03%. Deviations from the optimal matching load lead to worse matching, increasing the reflection and decreasing the conversion gain of the rectifier. Additional losses due to poor impedance matching are

also observed leading to only 18% and 22% peak PCE at RL = 50Ω and $1k\Omega$ respectively. While the reported peak PCE of 24.03% is lower than that of the above works, it is well-suited for the requirements of low-power IoT and sensor systems, emphasizing application simplicity, low cost, and comparably low form factors. Furthermore, achieving such an efficiency for 2.45 GHz is of significance, due to the Wi-Fi band's relatively small available ambient power when compared to sub-GHz ISM bands

5. Conclusions

The proposed RF energy harvesting (EH) system is developed for low-power applications and is composed of three main units: a microstrip patch antenna array with rectangular patches and a circular ground plane, an equal-power combiner, and a rectifier circuit that is impedance-matched to the load. The antenna array is designed to operate at 2.45 GHz; a frequency widely used in Wi-Fi. Simulations at this frequency show a realized gain of 4.055 dB. The radiation patterns obtained at the target frequency exhibit omni-directional characteristics. The array provides desirable performance in terms of wide bandwidth, omnidirectional radiation, and satisfactory realized gain, making it a promising candidate for energy harvesting. In addition, a circular equal-power combiner was designed to function at the same frequency to collect RF signals from the array, while the rectifier circuit converts the captured energy into DC. A carefully matched network was optimized and fabricated for the rectifier. System simulations were performed using both MATLAB and CST Microwave Studio software. Measurements using an HP8719Es VNA demonstrated good agreement with CST results, confirming the accuracy of the design approach. The fabricated prototype achieved a maximum RF-to-DC conversion efficiency of about 24.03% with a 200 Ω load and generated an output voltage of 250 mV. The functionality of the system was validated by powering an LED. Although the current prototype has a relatively large size due to employing FR-4 and Roger's substrates for testing, future work will concentrate on miniaturization and integration to enable use in compact IoT, wearable, and embedded devices.

References

- [1] Ibrahim, H. H., Singh, M. J., Al-Bawri, S. S., Ibrahim, S. K., Islam, M. T., Alzamil, A., & Islam, M. S. (2022). Radio Frequency Energy Harvesting Technologies: A Comprehensive Review on Designing, Methodologies, and Potential Applications. In Sensors (Vol. 22, Issue 11, p. 4144). MDPI AG.
- [2] Sanislav, T., Mois, G. D., Zeadally, S., & Folea, S. C. (2021). Energy Harvesting Techniques for Internet of Things (IoT). In IEEE Access (Vol. 9, pp. 39530–39549). Institute of Electrical and Electronics Engineers (IEEE)
- [3] Tran, LG., Cha, HK. & Park, WT. RF power harvesting: a review on designing methodologies and applications. Micro and Nano Syst Lett 5, 14 (2017).
- [4] Hwang, Y. M., Park, J. H., Shin, Y., Kim, J. Y., & Kim, D. I. (2017). Transmission Power and Antenna Allocation for Energy-Efficient RF Energy Harvesting Networks with Massive MIMO. Energies, 10(6), 802

- [5] Kabeel, A. A., Hussein, A. H., Khalaf, A. A. M., & Hamed, H. F. A. (2019). A utilization of multiple antenna elements for matched filter-based spectrum sensing performance enhancement in cognitive radio system. AEU - International Journal of Electronics and Communications, 107, 98-109.
- [6] Hany, H., Abdelatty, H., Kabeel, A., & Abdallah, R. (2024). Performance Analysis of Rectangular Microstrip Patch Antenna on Varied Substrates for RF Energy Harvesting Systems. In 2024 International Conference on Future Telecommunications and Artificial Intelligence (IC-FTAI) (pp. 1-5). 2024 International Conference on Future Telecommunications and Artificial Intelligence (IC-FTAI). IEEE. https://doi.org/10.1109/ic-ftai62324.2024.10950022.
- [7] Ahmed, R., Mohammed, Mohammed. A., & Kabeel, Ahmed. A. (2022). Characterization of tunable Ultra-Wideband Square Microstrip antenna with several gaps. In 2022 Telecommunications Conference (ITC-Egypt) (pp. 1-6). 2022 International Telecommunications Conference (ITC-Egypt). IEEE.
- [8] Hemour, S., Zhao, Y., Lorenz, C. H. P., Houssameddine, D., Gui, Y., Hu, C.-M., & Wu, K. (2014). Towards Low-Power High-Efficiency RF and Microwave Energy Harvesting. IEEE Transactions on Microwave Theory and Techniques, 62(4), 965–976. https://doi.org/10.1109/tmtt.2014.2305134
- [9] O. M. Ramahi, T. S. Almoneef, M. AlShareef, and M. S. Boybay, "Metamaterial particles for electromagnetic energy harvesting," Appl. Phys. Lett., vol. 101, no. 17, p. 173903, Oct. 2012, Doi: 10.1063/1.4764054.
- [10] B. Alavikia, T. S. Almoneef, and O. M. Ramahi, "Electromagnetic energy harvesting using complementary split-ring resonators," Appl. Phys. Lett., vol. 104, no. 16, p. 163903, Apr. 2014, Doi: 10.1063/1.4873587.
- [11] B. Alavikia, T. S. Almoneef, and O. M. Ramahi, "Complementary split ring resonator arrays for electromagnetic energy harvesting," Appl. Phys. Lett., vol. 107, no. 3, p. 033902, Jul. 2015, Doi: 10.1063/1.4927238.
- [12] M. Amiri, F. Tofigh, N. Shariati, J. Lipman, and M. Abolhasan, "Wide-angle metamaterial absorber with highly insensitive absorption for TE and TM modes," Sci. Rep., vol. 10, no. 1, pp. 1–13, 2020, Doi: 10.1038/s41598-020-70519-8.
- [13] M. L. Hakim, T. Alam, A. F. Almutairi, M. F. Mansor, and M. T. Islam, "Polarization insensitivity characterization of dual-band perfect metamaterial absorber for K band sensing applications," Sci. Rep., vol. 11, no. 1, pp. 1–15, 2021, Doi: 10.1038/s41598-021-97395-0.
- [14] M. Amiri, F. Tofigh, N. Shariati, J. Lipman, and M. Abolhasan, "Miniature tri-wideband Sierpinski-Minkowski fractals metamaterial perfect absorber," IET Microwaves, Antennas Propag., vol. 13, no. 7, pp. 991–996, 2019, Doi: 10.1049/iet-map.2018.5837.
- [15] A. A. G. Amer, S. Z. Sapuan, A. Alzahrani, N. Nasimuddin, A. A. Salem, and S. S. M. Ghoneim, "Design and Analysis of Polarization-Independent, Wide-Angle, Broadband Metasurface Absorber Using Resistor-Loaded Split-Ring Resonators," Electronics, vol. 11, no. 13, p. 1986, Jun. 2022, Doi: 10.3390/electronics11131986.
- [16] M. El Badawe, T. S. Almoneef, and O. M. Ramahi, "A metasurface for conversion of electromagnetic radiation to DC," AIP Adv., vol. 7, no. 3, p. 035112, Mar. 2017, Doi: 10.1063/1.4978321.
- [17] T. S. Almoneef, F. Erkmen, and O. M. Ramahi, "Harvesting the Energy of Multi-Polarized Electromagnetic Waves," Sci. Rep., vol. 7, no. 1, p. 14656, Dec. 2017, Doi: 10.1038/s41598-017-15298-5.
- [18] El Metaafy, H., Mohana, M., Gomaa, A., Yacoub, M. S., & Kassem, G. (2014). A PROPOSED DESIGN OF UWB MONOPOLE ANTENNA AND ITS LINEAR ARRAYS. JES. Journal of Engineering Sciences, 42(6), 1392–1413. https://doi.org/10.21608/jesaun.2014.115131
- [19] A. A. Ghaleb Amer, S. Z. Sapuan, and N. Nasimuddin, "Wide-Coverage Suspended Metasurface Energy Harvester for ISM Band Applications," in 2021 IEEE 19th Student Conference on Research and Development (SCOReD), Nov. 2021, pp. 87–90. Doi: 10.1109/SCOReD53546.2021.9652779.
- [20] A. A. G. Amer, S. Z. Sapuan, N. Nasimuddin, and M. F. Hassan, "A Broadband Wide-Angle Metasurface Absorber for Energy Harvesting Applications," 2021 Int. Conf. Technol. Sci. Adm. ICTSA 2021, no. April, 2021, Doi: 10.1109/ICTSA52017.2021.9406540.
- [21] J. Zhao and Y. Cheng, "Ultrabroadband Microwave Metamaterial Absorber Based on Electric SRR Loaded with Lumped Resistors," J. Electron. Mater., vol. 45, no. 10, pp. 5033-5039, Oct. 2016, Doi: 10.1007/s11664-016-4693-0.
- [22] K. P. Kaur, T. Upadhyaya, M. Palandoken, and C. Gocen, "Ultrathin dual-layer triple-band flexible microwave metamaterial absorber for energy harvesting applications," Int. J. RF Microw. Comput. Eng., vol. 29, no. 1, pp. 1–7, 2019, Doi: 10.1002/mmce.21646.

- [23] M. A. Aldhaeebi and T. S. Almoneef, "Double-sided metasurface array for a dual-band and polarization-independent microwave-energy-harvesting system," Materials (Basel)., vol. 14, no. 21, pp. 1–12, 2021, Doi: 10.3390/ma14216242.
- [24] H.-T. Zhong, X.-X. Yang, X.-T. Song, Z.-Y. Guo, and F. Yu, "Wideband metamaterial array with polarization-independent and wide incident angle for harvesting ambient electromagnetic energy and wireless power transfer," Appl. Phys. Lett., vol. 111, no. 21, p. 213902, Nov. 2017, Doi: 10.1063/1.4986320.
- [25] X. Duan, X. Chen, Y. Zhou, L. Zhou, and S. Hao, "Wideband Metamaterial Electromagnetic Energy Harvester with High Capture Efficiency and Wide Incident Angle," IEEE Antennas Wirel. Propag. Lett., vol. 17, no. 9, pp. 1617–1621, Sep. 2018, Doi: 10.1109/LAWP.2018.2858195.
- [26] A. Ghaneizadeh, M. Joodaki, J. Borcsok, A. Golmakani, and K. Mafinezhad, "Analysis, Design, and Implementation of a New Extremely Ultrathin 2-D-Isotropic Flexible Energy Harvester Using Symmetric Patch FSS," IEEE Trans. Microw. Theory Tech., vol. 68, no. 6, pp. 2108–2115, 2020, Doi: 10.1109/TMTT.2020.2982386.
- [27] B. Ghaderi, V. Nayyeri, M. Soleimani, and O. M. Ramahi, "Multi-polarisation electromagnetic energy harvesting with high efficiency," IET Microwaves, Antennas Propag., vol. 12, no. 15, pp. 2271–2275, Dec. 2018, Doi: 10.1049/iet-map.2018.5011.
- [28] X. Zhang, H. Liu, and L. Li, "Electromagnetic Power Harvester Using Wide-Angle and Polarization-Insensitive Metasurfaces," Appl. Sci., vol. 8, no. 4, p. 497, Mar. 2018, Doi: 10.3390/app8040497.
- [29] A. Ghaneizadeh, K. Mafinezhad, and M. Joodaki, "Design and fabrication of a 2D-isotropic flexible ultra-thin metasurface for ambient electromagnetic energy harvesting," AIP Adv., vol. 9, no. 2, p. 025304, Feb. 2019, Doi: 10.1063/1.5083876.
- [30] H.-T. Zhong, X.-X. Yang, C. Tan, and K. Yu, "Triple-band polarization-insensitive and wide-angle metamaterial array for electromagnetic energy harvesting," Appl. Phys. Lett., vol. 109, no. 25, p. 253904, Dec. 2016, Doi: 10.1063/1.4973282.
- [31] B. Ghaderi, V. Nayyeri, M. Soleimani, and O. M. Ramahi, "Pixelated Metasurface for Dual-Band and Multi-Polarization Electromagnetic Energy Harvesting," Sci. Rep., vol. 8, no. 1, p. 13227, Dec. 2018, Doi: 10.1038/s41598-018-31661-6.
- [32] Wei, Y., Duan, J., Jing, H., Yang, H., Deng, H., Song, C., Wang, J., Qu, Z., & Zhang, B. (2022). Scalable, Dual-Band Metasurface Array for Electromagnetic Energy Harvesting and Wireless Power Transfer. Micromachines, 13(10), 1712. https://doi.org/10.3390/mi13101712
- [33] L. Li, X. Zhang, C. Song, W. Zhang, T. Jia, and Y. Huang, "Compact Dual-Band, Wide-Angle, Polarization- Angle -Independent Rectifying Metasurface for Ambient Energy Harvesting and Wireless Power Transfer," IEEE Trans. Microw. Theory Tech., vol. 69, no. 3, pp. 1518–1528, 2021, Doi: 10.1109/TMTT.2020.3040962.
- [34] K. Lee and S. K. Hong, "Rectifying Metasurface with High Efficiency at Low Power for 2.45 GHz Band," IEEE Antennas Wirel. Propag. Lett., vol. 19, no. 12, pp. 2216–2220, Dec. 2020, Doi: 10.1109/LAWP.2020.3027833.
- [35] M. El Badawe and O. M. Ramahi, "EFFICIENT METASURFACE RECTENNA FOR ELECTROMAGNETIC WIRELESS POWER TRANSFER AND ENERGY HARVESTING," Prog. Electromagn. Res., vol. 161, no. January, pp. 35–40, 2018, Doi: 10.2528/PIER18011003.
- [36] P. Xu, S.-Y. Wang, and W. Geyi, "Design of an effective energy receiving adapter for microwave wireless power transmission application," AIP Adv., vol. 6, no. 10, p. 105010, Oct. 2016, Doi: 10.1063/1.4966050.
- [37] X. Zhang, H. Liu, and L. Li, "Tri-band miniaturized wide-angle and polarization-insensitive metasurface for ambient energy harvesting," Appl. Phys. Lett., vol. 111, no. 7, p. 071902, Aug. 2017, Doi: 10.1063/1.4999327.
- [38] N. N. Yoon, N. Ha-Van, and C. Seo, "High-gain and wideband aperture coupled feed patch antenna using four split ring resonators," Microw. Opt. Technol. Lett., Aug. 2018.
- [39] Y. Luo, L. Pu, G. Wang, and Y. Zhao, "RF Energy Harvesting Wireless Communications: Rf Environment, Device Hardware and Practical Issues," Sensors, 2019.
- [40] U. Özkaya, L. Seyfi and Ş. Öztürk, "Çoklu banda sahip mikroşerit antenlerde boyut optimizasyonunun derin öğrenme yöntemleri ile gerçekleştirilmesi" Pamukkale Üniversitesi Mühendislik Bilimleri Dergisi, 27(2), 229-233, 2021.
- [41] A. Mohan and S. Mondal, "An impedance matching strategy for micro-scale RF energy harvesting systems," IEEE Transactions on Circuits and Systems II: Express Briefs, 2020
- [42] Khemar, A., Kacha, A., Takhedmit, H., & Abib, G. "Design and experiments of a dual-band rectenna for ambient RF energy harvesting in urban environments," IET Microwaves, Antennas & Propagation, 2017.

- [43] S. Shrestha, S.K. Noh, and D.Y. Choi, "Comparative Study of Antenna Designs for RF Energy Harvesting," Int. J. Antennas Propagation, vol. 2013, Feb. 2013.
- [44] Liu, X.; Li, M.; Chen, X.; Zhao, Y.; Xiao, L.; Zhang, Y. A Compact RF Energy Harvesting Wireless Sensor Node with an Energy Intensity Adaptive Management Algorithm. Sensors **2023**, 23, 8641.
- [45] Kadir, E.A.; Hu, A.P.; Biglari-Abhari, M.; Aw, K.C. Indoor Wi-Fi Energy Harvester with Multiple Antenna for Low-Power Wireless Applications. In Proceedings of the 2014 IEEE 23rd International Symposium on Industrial Electronics (ISIE), Istanbul, Turkey, 1–4 June 2014; pp. 526–530.
- [46] DeLong, B.J.; Kiourti, A.; Volakis, J.L. A Radiating Near-Field Patch Rectenna for Wireless Power Transfer to Medical Implants at 2.4 GHz. IEEE J. Electromagn. RF Microw. Med. Biol. **2018**, 2, 6
- [47] Kim, S.; Bito, J.; Jeong, S.; Georgiadis, A.; Tentzeris, M.M. A Flexible Hybrid Printed RF Energy Harvester Utilizing Catalyst- Based Copper Printing Technologies for Far-Field RF Energy Harvesting Applications. In Proceedings of the 2015 IEEE MTT-S International Microwave Symposium, Phoenix, AZ, USA, 17–22 May 2015; pp. 1–4.
- [48] Liu, X.; Li, M.; Chen, X.; Zhao, Y.; Xiao, L.; Zhang, Y. A Compact Stacked RF Energy Harvester with Multi-Condition Adaptive Energy Management Circuits. Micromachines **2023**, 14, 1967.
- [49] Li, P.; Long, Z.; Yang, Z. RF Energy Harvesting for Batteryless and Maintenance-Free Condition Monitoring of Railway Tracks. IEEE Internet Things J. **2021**, 8, 3512–3523.
- [50] Loubet, G.; Takacs, A.; Dragomirescu, D. Implementation of a Battery-Free Wireless Sensor for Cyber-Physical Systems Dedicated to Structural Health Monitoring Applications. IEEE Access **2019**, 7, 24679–24690.
- [51] Khan, N.U.; Ullah, S.; Khan, F.U.; Merla, A. Development of 2400–2450 MHz Frequency Band RF Energy Harvesting System for Low-Power Device Operation. Sensors 2024, 24, 2986. https://doi.org/10.3390/s241029